



Spatial separation of photogenerated carriers and enhanced photocatalytic performance on Ag₃PO₄ catalysts via coupling with PPy and MWCNTs

Yan Lin^{a,1}, Xin Wu^{a,1}, Yi Han^{a,1}, Chunping Yang^{a,b,*}, Yin Ma^b, Cheng Du^b, Qing Teng^b, Hongyu Liu^a, Yuanyuan Zhong^b

^a College of Environmental Science and Engineering, Hunan University and Key Laboratory of Environmental Biology and Pollution Control (Hunan University), Ministry of Education, Changsha, Hunan 410082, China

^b Guangdong Provincial Key Laboratory of Petrochemical Pollution Processes and Control, School of Environmental Science and Engineering, Guangdong University of Petrochemical Technology, Maoming, Guangdong 525000, China



ARTICLE INFO

Keywords:

Ag₃PO₄-based catalyst
Photogenerated carrier
Multi-walled carbon nanotube (MWCNTs)
Polypyrrole (PPy)
Photocatalysis

ABSTRACT

Visible-light-driven photocatalysis is a promising technology in the environmental pollutant remediation, and charge separation is crucial for increasing the activity of photocatalysts. In this study, novel photocatalysts Ag₃PO₄@MWCNTs@PPy with excellent photocatalytic activity and photostability were successfully synthesized. The results of density functional theory (DFT) calculation and photochemical deposition experiments demonstrated that a spatial separation system of photogenerated carriers in Ag₃PO₄@MWCNTs@PPy composite was successfully constructed. The photogenerated electrons of Ag₃PO₄ were readily transferred to MWCNTs and the photogenerated holes tended to migrate to the surface of PPy, resulting in superior separation efficiency of photogenerated carriers and great enhancement of photocatalytic activity. The photocatalytic degradation efficiency of phenol and tetracycline hydrochloride (TC) over optimal ternary catalyst could reach 100% with visible light irradiation for 20 min and 5 min, respectively. Simultaneously, 80.12% of TOC removal efficiency was also achieved within 20 min on the mineralization of phenol. The LC-MS and 3D EEMs (three-dimensional excitation-emission-matrix spectra) analyses showed that TC was mainly degraded into small molecule acids, fulvic acids- and humic acids-like matters. In addition, a new method of preparing Ag₃PO₄ with uniform small-sized particles was proposed, by which the large Ag₃PO₄ polyhedron crystals with a diameter of 10–25 μm were transformed into particles in a range of 0.2–1.4 μm in diameter, and the apparent rate constant of phenol degradation by this small-sized Ag₃PO₄ was 3.8 times of that by the large-sized. In this work a new photocatalyst with great application potential has been fabricated, and the strategy for constructing the carrier spatial separation system is promising and intriguing for designing high efficient photocatalysts.

1. Introduction

Over the past several decades, there have been increasing concerns about environmental pollution and energy shortage [1,2]. Photocatalysis is considered as one of the most promising technologies to address these concerns [3,4]. The exploration of novel photocatalysts with good stability and high catalytic efficiency under visible light is a core issue in photocatalysis [5–7]. Among the photocatalysts reported, silver phosphate (Ag₃PO₄) is considered an ideal candidate for organic pollutant degradation due to its highly positive valence band position, low-toxicity, and excellent photocatalytic ability [8,9]. Despite the fact that Ag₃PO₄ exhibits high efficient photocatalytic performance under

visible light, there are still some limitations that hinder its wide applications. One disadvantage is that Ag₃PO₄ crystals tend to form large-sized polyhedral particles in the growth process [10]. Charge carriers travel longer distance to the surface in large-sized photocatalyst than that in smaller ones, resulting in a large number of bulk electron-hole recombination and reduced photocatalytic performance. In addition, the photogenerated electrons could cause easy reduction of Ag⁺ into metallic Ag and the recombination of photogenerated charges during the photocatalytic process, resulting in the photocorrosion of Ag₃PO₄ and reduction in photocatalytic activity [11].

In order to overcome the above shortcomings, enormous efforts have been devoted. On the one hand, it was imperative to optimize the

* Corresponding author at: College of Environmental Science and Engineering, Hunan University, Changsha, Hunan 410082, China.

E-mail address: yangc@hnu.edu.cn (C. Yang).

¹ These authors contribute equally to this paper.

morphology and particle size of Ag_3PO_4 . The improvements in the preparation process of photocatalyst were therefore considered [12–14]. For example, Ag_3PO_4 nanocrystals with controlled particle size have been synthesized using an oleylamine-assisted method, which exhibited superior photocatalytic activity under visible light as compared to that of large-sized Ag_3PO_4 particles [15]. Wang et al. also provided a soft chemical method to synthesize Ag_3PO_4 crystals with various new morphologies, including branch, tetrapod, nanorod and triangular prism, by adjusting static and ultrasonic conditions. Because of smaller particle size and larger specific surface area, higher photodegradation activity was obtained [16]. The above reports revealed that size control and morphology transformation were effective way to improve the catalytic activity of Ag_3PO_4 . However, there were some deficiencies in these preparation methods, such as complicated steps or difficult conditions to adjust, so it was necessary to develop facile and easy-to-operate synthetic methods. Herein, small-sized Ag_3PO_4 crystals with uniform particle size were successfully synthesized by adjusting phosphorus source and controlling droplet dropping speed.

On the other hand, charge separation plays an important role in improving photocatalytic performance and inhibiting photocorrosion of Ag_3PO_4 . Since all photocatalytic reactions occur on the surface of photocatalyst, as a key step in energy conversion, electron-hole pairs generated by light absorption need to be separated and transferred to the surface of the photocatalyst [12,17]. Therefore, there were also studies on the design and construction of charge spatial separation system. For example, Domen et al. synthesized the core/shell Ta_3N_5 photocatalysts with spatially separated cocatalysts to improve the photocatalytic activity, and the high activity was attributed to the separation and migration of photogenerated electrons and holes toward the inner and outer surfaces of catalyst respectively [18]. A ternary $\text{TiO}_2\text{-MnO}_x\text{-Pt}$ photocatalyst was also prepared, the hole-rich {001} facets and electron-rich {101} facets of TiO_2 formed a surface heterojunction, which spatially separated the photogenerated electrons and holes to different facets, and then migrated to Pt and MnO_x , respectively [19]. Similarly, the efficient charge separation could be achieved on different crystal facets of BiVO_4 and SrTiO_3 , and the reduction and oxidation cocatalysts were selectively deposited on the different facets respectively, leading to much higher photocatalytic activity [17,20].

Obviously, the above successful cases proved that if the photo-induced electrons and holes generated in the catalyst bulk phase could be actively rectified to different directions, the efficient spatial separation of photogenerated charges and excellent catalytic activity would be achieved. Another key point was to select good conductors and collectors for photogenerated electrons and holes. Multi-walled carbon nanotubes (MWCNTs) have became one of the most promising materials due to their fascinating properties of high electrical conductivity, excellent electron acceptor properties, flexibility of modulating the specific surface area, impressive mechanical and thermal stabilities, and tolerance against poisoning effect [21]. Thus, MWCNTs as the excellent acceptors and conductors of photogenerated electrons have been selected as good additives for photocatalyst modification. In particular, our previous studies have shown that the photogenerated electrons of Ag_3PO_4 could be rapidly migrated to the surface of catalyst through MWCNTs, and the significant enhancement of photocatalytic performance and inhibition of photocorrosion were thus achieved. Hence, in present work, MWCNTs were also chosen as the conductors and collectors for photogenerated electrons [22]. On this basis, we focused on hybridizing Ag_3PO_4 @MWCNTs with other materials to construct a spatial separation system of photogenerated carriers.

Polypyrrole (PPy) is one of the π -conjugated heterocyclic conducting polymer with advantages of high conductivity, good environment stability, outstanding carrier mobility, excellent electrochemical activity and facile synthesis [23,24]. Recently, a few studies have focused on employing pure PPy as photocatalyst for water depollution or combining PPy with other catalysts to improve the photocatalytic performance [23,25]. For instance, the photocatalytic activity of $\text{g-C}_3\text{N}_4$

nanosheet, Ta_3N_5 and TiO_2 [26] was significantly improved after coupling with PPy. Liang et.al reported that photogenerated holes of $\text{g-C}_3\text{N}_4$ could be transferred to the PPy for oxidation of phenol and other organic pollutants [27]. The Ta_3N_5 /PPy composite exhibited very high photocatalytic activity for overall water splitting because the generated holes of Ta_3N_5 could be quickly transferred to the PPy surface, where they cannot oxidize the nitrogen anions. Thus, the introduction of PPy could not only inhibit the recombination of photogenerated electrons and holes, but also effectively prevent the self-photocorrosion of Ta_3N_5 photocatalysts [28]. These successful cases demonstrated that PPy could serve as the trapping center and transport material for photogenerated holes, improving the mobility of holes and inducing the separation of electron-hole pair, and consequently the catalytic activity of the photocatalysts was enhanced. Therefore, in consideration of the unique excellent characteristic of PPy and MWCNTs, MWCNTs and PPy were selected as conductors and collectors for photogenerated electrons and holes, respectively. A spatial separation system of photogenerated carriers was expected to be constructed, thus enhancing the photocatalytic performance and photostability of Ag_3PO_4 .

Unfortunately, to the best of our knowledge, the novel Ag_3PO_4 @MWCNTs@PPy composite photocatalyst that should have superior photocatalytic performance and photostability has not been reported. Besides, data proof and reports on the construction of spatial separation system for photogenerated carriers in Ag_3PO_4 are not available. Herein, the new photocatalyst Ag_3PO_4 @MWCNTs@PPy was synthesized for the first time. In addition, the spatial separation system of photogenerated carriers in Ag_3PO_4 @MWCNTs@PPy composite was constructed and proved firstly by the DFT calculation and photochemical deposition experiments. A new method was also proposed to prepare small-sized Ag_3PO_4 with uniform particles. The photocatalytic activities and photostability of photocatalysts were evaluated by degradation of phenol and TC, and its mineralization ability was determined by TOC removal efficiency. The photodegradation products and pathway of TC were analyzed by LC-MS and 3D EEMs technologies. The ESR and radical trapping experiments were conducted to investigate the photodegradation mechanisms. This study proposed a new design scheme to construct high efficient solar energy conversion systems with great potential to improve the catalytic performance of photocatalysts.

2. Experimental section

2.1. Materials

Preparation of Ag_3PO_4 , Ag_3PO_4 @MWCNTs, Ag_3PO_4 @PPy and Ag_3PO_4 @MWCNTs@PPy

The chemicals and preparation of samples are available in the supporting information.

2.2. Characterization

Field emission scanning electron microscopy (FESEM, Hitachi SU8220, Japan) and high resolution transmission electron microscope (HRTEM) (TecnaiG2 F20, FEI, USA) were employed to investigate the morphologies and microstructures of samples. The crystal structures of the prepared samples were characterized by X-ray diffractometer (Bruker AXS D8 Advances, Germany) with the Cu-K α radiation ($\lambda=0.15406$ nm). Chemical compositions of samples were analyzed using X-ray photoelectron spectroscopy (XPS, ESCALAB 250Xi, Thermo Fisher, USA). The UV-vis diffused reflectance spectra (UV-vis DRS) were obtained by UV-vis-NIR spectrophotometer (U-4100, Hitachi, Japan). The photoluminescence (PL) spectra were studied through photoluminescence spectrometer (HORIBA Scientific, iHR320). Raman spectra were obtained on a confocal micro-Raman spectrometer (Horiba Jobin Yvon LabRAM HR800) with an excitation of 633 nm laser light. The BET specific surface of the samples was determined by surface area porosity analyzer (Micromeritics, TriStar II 3020, USA). The

photocurrent response curve and Mott-Schottky plots of the prepared samples were measured by a three-electrode cell in 0.5 mol/L Na₂SO₄ aqueous solution and a CHI 760E workstation. The as-prepared photocatalysts thin film on fluorine-doped tin oxide (FTO) was used as the working electrode. The other two electrodes were a saturated calomel reference electrode saturated calomel electrode (SCE) and a platinum (Pt) electrode, respectively. The electron spin resonance (ESR) signals of radicals spin-trapped by spin-trapped reagent 5, 5-dimethyl-l-pyrrolidine N-oxide (DMPO) were examined on a JES FA200 electron paramagnetic resonance spectrometer under visible light irradiation ($\lambda > 420$ nm). The mineralization ability was tested by total organic carbon (TOC) measurements (Shimadzu TOC-VCPh analyzer). 3D EEMs were examined by an F-4500 spectrofluorimeter, and the excitation (λ_{ex}) and emission wavelengths (λ_{em}) were 200–500 and 200–550 nm, respectively.

2.3. Photoreaction procedures

The photocatalytic activity of the obtained samples was evaluated by phenol and TC decomposition under visible light irradiation. A 300 W Xe lamp with a 420 nm cutoff filter was employed as the light source. The reaction system was cooled and maintained at room temperature by circulating tap water. In a typical procedure, 50 mg photocatalyst was dispersed in the reaction solution (100 mL, 20 mg/L phenol or TC). The mixed solution was stirred in dark for 30 min to reach the adsorption-desorption equilibrium. Afterwards, the suspension was exposed to the 300 W Xe lamp. 1 mL of suspension was taken out at a given interval time, and then filtrated through a 0.22 µm Millipore filter to remove the particles. The residual concentration was analyzed by high performance liquid chromatography (HPLC, Agilent, USA) equipped with a UV detection and an Agilent ZORBAX SB-C18 (5 µm × 4.6 mm × 250 mm) reversed-phase column. The detector was set at the wavelength of 270 nm and 360 nm for phenol and TC, respectively. The operating conditions were as follows: the mobile phase of phenol and TC were methanol and water (volume ratio: 40/60), and 0.01 M formic acid and acetonitrile (volume ratio: 80/20), respectively; flow rate at 1 mL/min; injection volume by 20 mL and column temperature of 30 °C. The degradation intermediates of TC were identified by a LC-MS system (6470 Triple Quad, Agilent) equipped with a Kromasil C18 column (250 × 4.6 mm, 5 µm). The elution was performed via 0.1% (v/v) of formic acid aqueous solution (A) and acetonitrile (B) at a flow rate of 0.2 mL/min. The injection volume was 2 µL, and the column temperature was 30 °C. Linear gradient elution was as follows: the initial 90% A was reduced to 10% A over 10 min and kept 4 min. Then the mobile phase A returned to 90% in 1 min and maintained 1 min. MS was conducted in the positive ion mode using an electrospray ionization (ESI) source under the following conditions: capillary voltage, 4.0 kV; gas (N₂) flow rate, 11 L/min; gas temperature, 300 °C; nebulization pressure, 15 psi. MS was scanned by mass range from 50 to 500 m/z.

2.4. Photo-deposition of platinum and manganese oxide

The photo-deposition of Pt was obtained using H₂PtCl₆·6H₂O as precursor. Briefly, 0.15 g Ag₃PO₄@MWCNTs powder was dispersed with 150 mL de-ionized water. The suspension was then irradiated with a 300 W Xe lamp under stirring after adding 1.0 mL of H₂PtCl₆·6H₂O solution (10 mg/mL). The photo-deposition of the MnO_x was obtained by using MnSO₄ and NaIO₃ as precursors and photogenerated electron acceptors, respectively. Similarly, 0.15 g Ag₃PO₄@PPy sample was dispersed with NaIO₃ solution (150 mL, 0.1 M). The MnSO₄ solution (1 mL, 10.0 mg/mL) was then added to the above dispersions and irradiated with 300 W Xe lamp. After 30 min of illumination, the precipitate were collected by centrifugation, washed with de-ionized water and ethanol, and dried in vacuum (55 °C) overnight. The as-obtained powder was used for characterizations.

2.5. Calculation details and computational models

All the density functional theory (DFT) calculations were performed using the Vienna ab-initio simulation package (VASP). The projector-augmented wave (PAW) method was used to represent the core-valence interaction. The plane wave energy cutoff was set to 450 eV. The exchange functional utilized is the GGA-PBE with the van der Waals corrections (zero damping DFT-D3 method of Grimme). The Brillouin zone was sampled at Gamma point with the 1 × 1 × 1 k-point mesh. The energy and force criterion for convergence of the electron density are set at 10⁻⁵ eV and 0.05 eV/Å, respectively.

For the Ag₃PO₄, the 2 × 2 (100) surface (a = b = 12.096 Å) was chosen to model the Ag₃PO₄, because it is the most stable one among the low index surfaces. The model contains 64 atoms (24 Ag, 8 P and 32 O atoms). The armchair (4, 4) was utilized to model the CNTs with the diameter of 5.42 Å. This nanotube with five repeat units (containing 80 atoms), and 1.6% compressed deformation along the z-axis direction were chosen to match Ag₃PO₄ (100) surface. For the PPy, five repeat pyrrole monomers were added on the Ag₃PO₄ (100) surface with 40 atoms (containing 20 C, 5 N and 15 H). The CNTs were located at one side of Ag₃PO₄ surface, while PPy was located on the other side of Ag₃PO₄ surface. The final MWCNTs@Ag₃PO₄@PPy model could be found in Fig. S1. A vacuum gap of 12 Å was used to avoid the interaction between the periodic slabs.

3. Results and discussion

3.1. Photocatalysts characterization

The morphology and structure of prepared samples were firstly characterized by FESEM. As shown in Fig. 1a, Ag₃PO₄ presented as an irregular sphere-like polyhedral morphology with a diameter of about 24 µm, and some small irregular particles were attached to it. The detailed synthetic method was referred to our previously report [22]. The results indicated that Ag₃PO₄ readily to form large-sized and irregular polyhedron structures in the preparation process [8]. To overcome this shortcoming, a new method was provided to prepare uniform small-sized Ag₃PO₄ particles. As shown in Fig. 1b, the large Ag₃PO₄ particles with a diameter of 10–25 µm could not be found, and particle size analysis of 412 particles was conducted (Fig. 1c). The particle size of Ag₃PO₄ ranged from 0.2 to 1.4 µm, of which about 69% ranged from 0.4 to 0.8 µm. The results showed that the particle size of Ag₃PO₄ could be effectively controlled by the proposed preparation method. Our previous studies have proved that MWCNTs could effectively increase the photogenerated electron migration rate of Ag₃PO₄ [22]. In order to further improve the photogenerated charge separation performance of modified pure Ag₃PO₄, MWCNTs were thus introduced into the system. The SEM images of Ag₃PO₄@MWCNTs composite were presented in Fig. 1d and e. It could be clearly seen that MWCNTs were uniformly coated on the surface of Ag₃PO₄ or penetrated into the Ag₃PO₄ crystals. This could be attributed to the electrostatically-driven self-assembly between Ag⁺ and negatively charged MWCNTs [8,10,11]. The SEM images of Ag₃PO₄@PPy composite shown in Fig. 1f and g indicated that PPy and Ag₃PO₄ were bound closely. The SEM in Fig. S2a showed that the raw PPy presented stacked and layered structure, and it was transformed into a thinner flaky structure after 16 h ultrasonic exfoliation, which could contribute to increasing the direct contact area between Ag₃PO₄ and PPy, and thus enhancing the photogenerated carrier transfer between them. As shown in Fig. 1h and i, both MWCNTs and PPy could be clearly seen in the Ag₃PO₄@MWCNTs@PPy composite, and Ag₃PO₄ crystals coated with MWCNTs grew on the flaky PPy, indicating good affinity among these materials. Obviously, the observations of SEM indicated that this new synthesis method of Ag₃PO₄ could control the size of crystal particles, PPy and MWCNTs were successfully incorporated into this system, and good interface contact among them was also established.

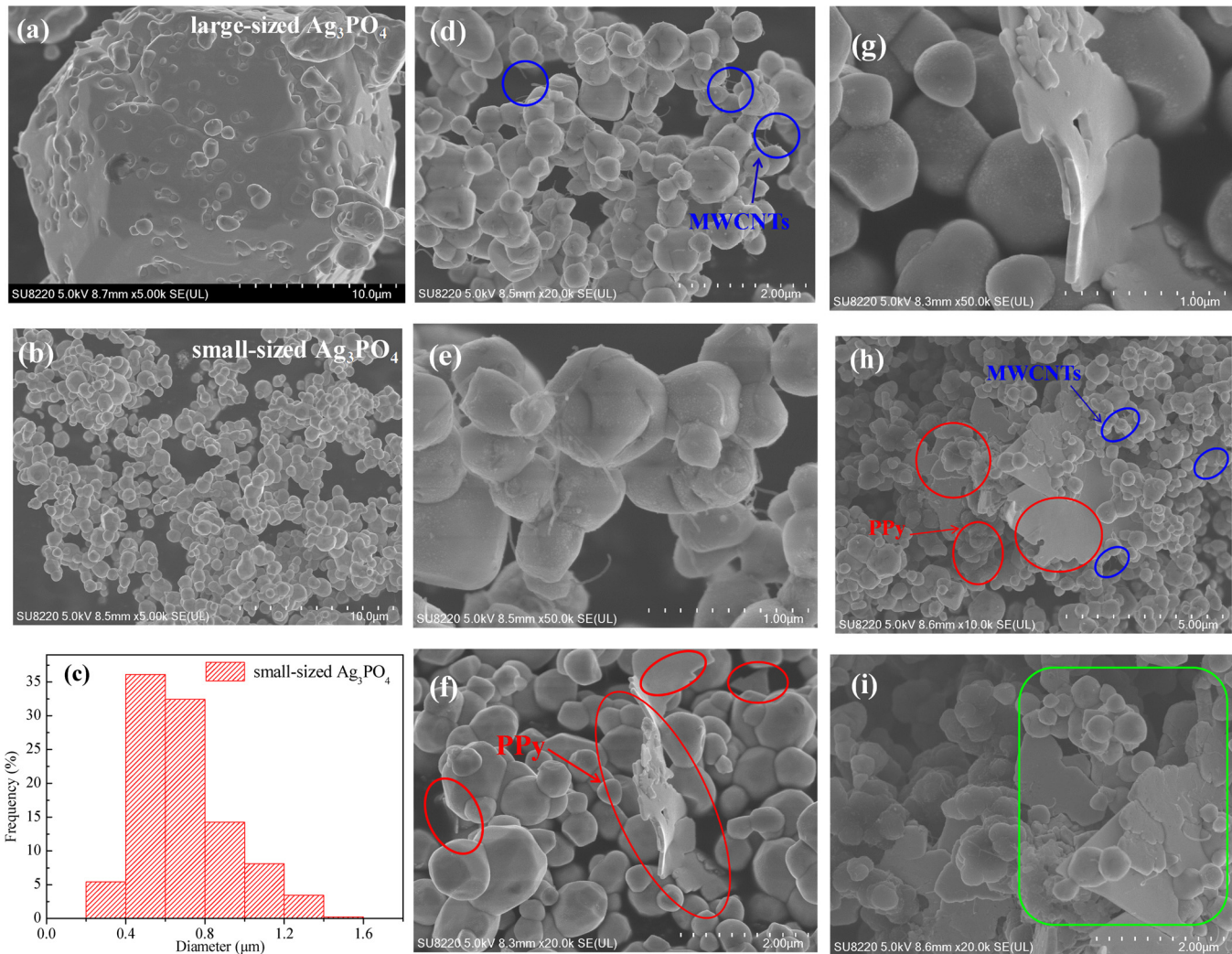


Fig. 1. SEM images of large-sized Ag_3PO_4 (a), small-sized Ag_3PO_4 (b), particle size distribution of small-sized Ag_3PO_4 (c), Ag_3PO_4 @MWCNTs composite (d,e), Ag_3PO_4 @PPy composite (f,g) and Ag_3PO_4 @MWCNTs@PPy composite (h,i).

The EDS analysis of Ag_3PO_4 @MWCNTs@PPy composite was performed and its results were provided in Fig. 2, which indicated the existence of Ag, O, C, P and N elements in the sample and the Ag_3PO_4 particles were adhered well on the surface of PPy. Besides, the high-resolution TEM (HRTEM) analysis was carried out to obtain more detailed information on the structure and morphology of photocatalysts. As presented in Figs. 3a, d and S2b, both the hollow MWCNTs and amorphous PPy could be clearly observed. MWCNTs with an outer diameter of about 20 nm coated on or penetrated through the Ag_3PO_4 particles, and close interfacial contact between PPy and Ag_3PO_4 could also be clearly seen. The selected area electron diffraction pattern (SAED) of Ag_3PO_4 in Ag_3PO_4 @MWCNTs@PPy composite was shown in Fig. 3b, and the clear diffraction rings revealed the crystalline nature of Ag_3PO_4 . The radius of diffraction rings was determined and the interplanar spacing was also calculated. The above results showed that the lattice structure of the crystal was body-centered cubic, and the continuous diffraction ring corresponded to the (110), (200), (211), (220) and (310) planes in turn. Moreover, the interplanar spacing of 0.269 and 0.245 nm were clearly observed in Fig. 3c, which correspond to (210) and (211) crystal planes of Ag_3PO_4 , respectively, and this was in agreement with the JCPDS card No. 06-0505. And the outer and inner walls of MWCNTs with carbon layer in the middle were marked with the blue solid line and dashed line, respectively (Fig. 3c). The results further conformed that the good binding among Ag_3PO_4 , MWCNTs and PPy in the Ag_3PO_4 @MWCNTs@PPy composite was built.

Due to the introduction of MWCNTs and PPy with large specific surface area, and the obviously reduced sizes of Ag_3PO_4 prepared by the new method, the BET specific surface area of different catalysts were thus measured (Table S1). The BET specific surface area of the large-sized Ag_3PO_4 , small-sized Ag_3PO_4 , Ag_3PO_4 @MWCNTs, Ag_3PO_4 @PPy and Ag_3PO_4 @MWCNTs@PPy were 0.1793, 0.9575, 1.9473, 1.2916 and 1.8651 m^2/g , respectively. Compared to the large-sized Ag_3PO_4 , the specific surface area of small-sized Ag_3PO_4 prepared by new synthetic method was increased obviously. After the introduction of MWCNTs and PPy, the specific surface area of Ag_3PO_4 @MWCNTs, Ag_3PO_4 @PPy and Ag_3PO_4 @MWCNTs@PPy was further increased. Especially, the specific surface area of Ag_3PO_4 @MWCNTs was twice that of small-sized Ag_3PO_4 , which was due to the large surface area of MWCNTs [30]. Therefore, more active species and pollutant molecules could be adsorbed on catalysts, which was conducive to improving its photocatalytic activity.

The crystal structure and phase of prepared samples was investigated by XRD. As shown in Fig. 4, all of the diffraction peaks for the pure Ag_3PO_4 , Ag_3PO_4 @MWCNTs, Ag_3PO_4 @PPy and Ag_3PO_4 @MWCNTs@PPy could be indexed to the body-centered cubic structure of Ag_3PO_4 (JCPDS No. 06-0505), which was consistent with the SAED result. No characteristic diffraction peaks for PPy was observed in Ag_3PO_4 @PPy and Ag_3PO_4 @MWCNTs@PPy composite, ascribing the PPy in the composites was amorphous [31]. The characteristic peak at 2θ value of 26.2° and 42.2° could be attributed to the (002) and (100)

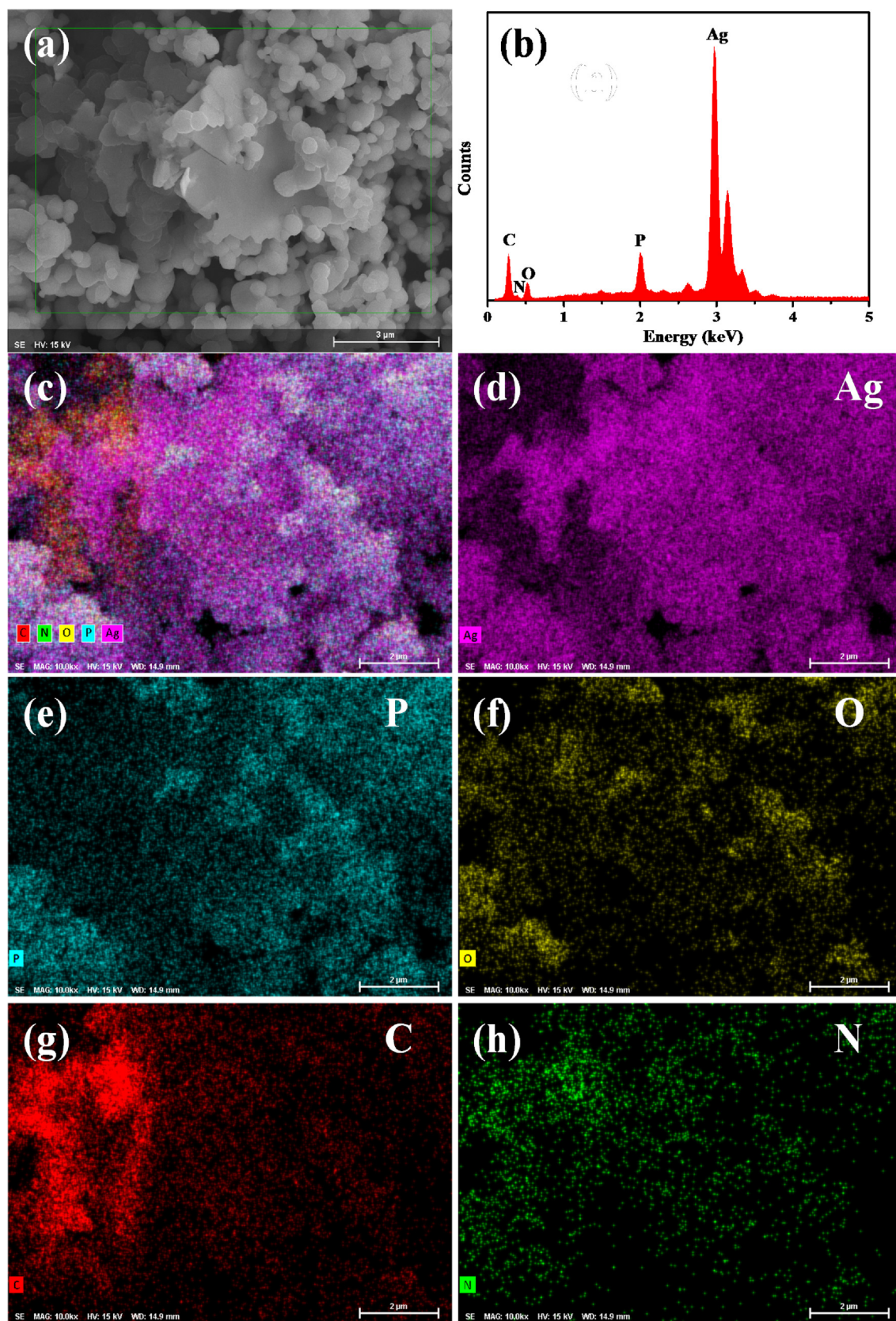


Fig. 2. SEM-EDS elemental mapping images of Ag_3PO_4 @MWCNTs@PPy composite.

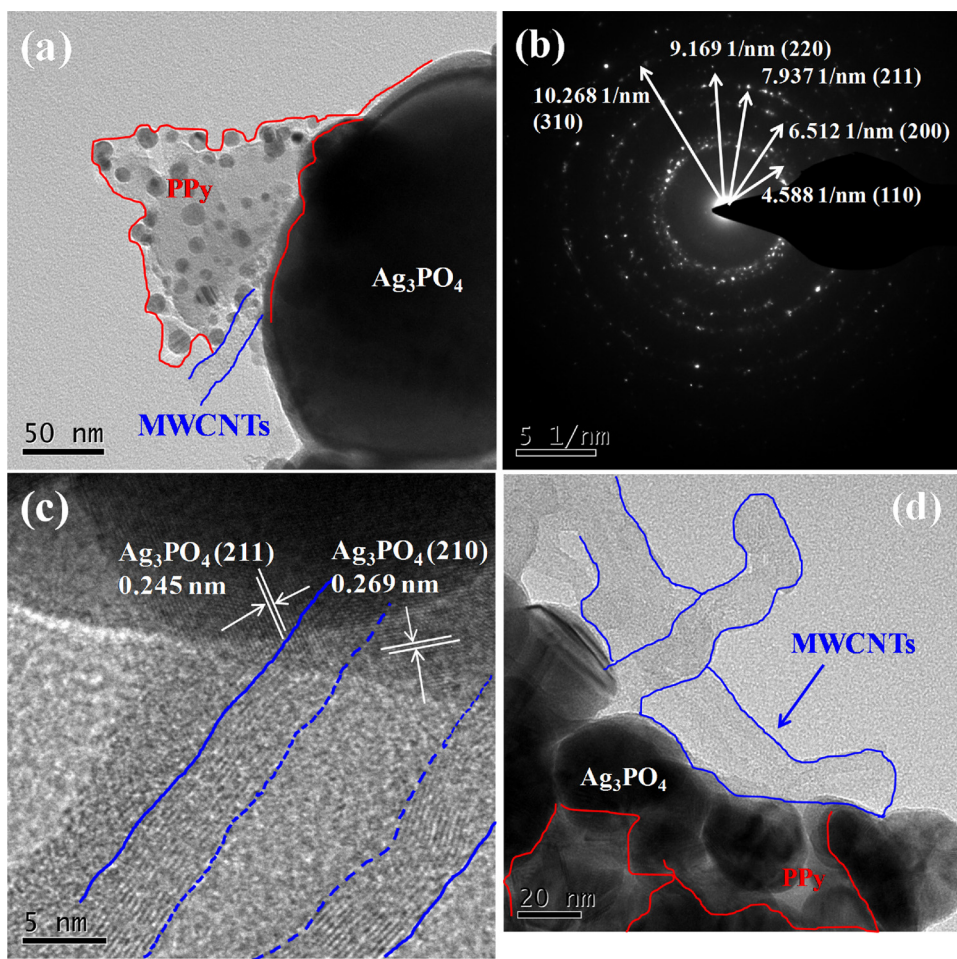


Fig. 3. HRTEM images analysis of Ag_3PO_4 @MWCNTs@PPy composite (a,c,d), SAED of Ag_3PO_4 (b).

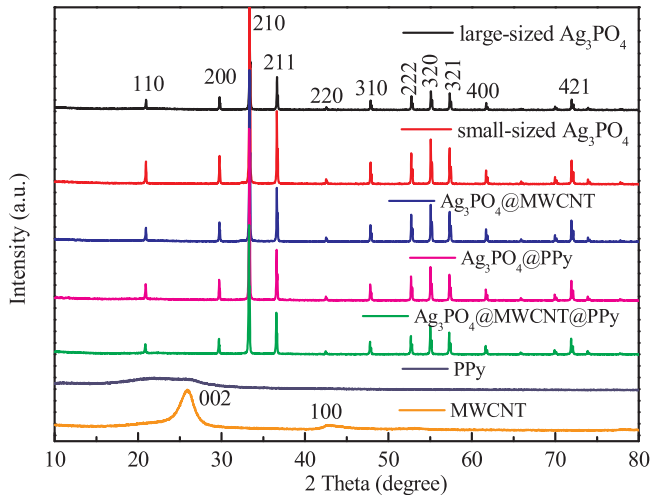


Fig. 4. XRD pattern of as-prepared samples.

plane of graphitized MWCNTs, respectively. The peaks belonging to MWCNTs in Ag_3PO_4 @MWCNTs and Ag_3PO_4 @MWCNTs@PPy could not be clearly observed because of the fairly low amount and the relatively low diffraction intensity of MWCNTs [8]. Although the positions of diffraction peaks for Ag_3PO_4 in different samples were almost the same, the intensity ratios of the peaks varied significantly. It was reported that the obvious change of characteristic peak intensity ratio implied the changes of the crystal facet exposure [9], and it was found that the

{111} facet of Ag_3PO_4 possessed considerably higher surface energy (1.65 J/m^2) than either {110} or {100} (0.78 and 0.67 J/m^2 respectively) [12]. The {111} diffraction peak could not be directly observed due to the reflection conditions of the space group. Similarly, {100} cannot be seen either [32]. So the {111} and {100} facet were presented as (222) and (200) facet on XRD patterns, respectively. The photocatalyst with higher surface energy facets exhibited higher activity and photocatalytic performance, which contributed to the decomposition of organic pollutants. Therefore, the peak intensity of (222) and (110) in different samples were concerned and their ratios were also calculated. The intensity ratio of the (222) and (110) peaks are 1.08:1, 1.34:1, 1.88:1, 1.73:1 and 2.06:1 for the large-sized Ag_3PO_4 , small-sized Ag_3PO_4 , Ag_3PO_4 @MWCNTs, Ag_3PO_4 @PPy and Ag_3PO_4 @MWCNTs@PPy, respectively. These results indicated that the exposing facets of Ag_3PO_4 were affected by the coupling with PPy and MWCNTs, and a higher proportion of (222) facet was formed during the growth of Ag_3PO_4 crystal, which contributed to the enhancement of photocatalytic activity.

X-ray photoelectron spectroscopy (XPS) analysis of Ag_3PO_4 and Ag_3PO_4 @MWCNTs@PPy was carried out to reveal the elemental chemical status and detailed information about the interaction among Ag_3PO_4 , MWCNTs and PPy. As shown in Fig. 5a, all signals of Ag, P, O, C and N were clearly observed in the XPS spectrum of Ag_3PO_4 @MWCNTs@PPy, which was consistent with the EDS result. It was found that the peaks of $\text{Ag } 3d_{3/2}$ and $\text{Ag } 3d_{5/2}$ were located at 367.7 eV and 373.7 eV, respectively, which could be ascribed to Ag^{+} in the Ag_3PO_4 (Fig. 5b). The spectrum in Fig. 5c indicated that the typical peak of P 2p located at 132.6 eV, which was in agreement with the phosphorus in PO_4^{3-} . As presented in Fig. 5d, the O 1s spectrum could be divided into

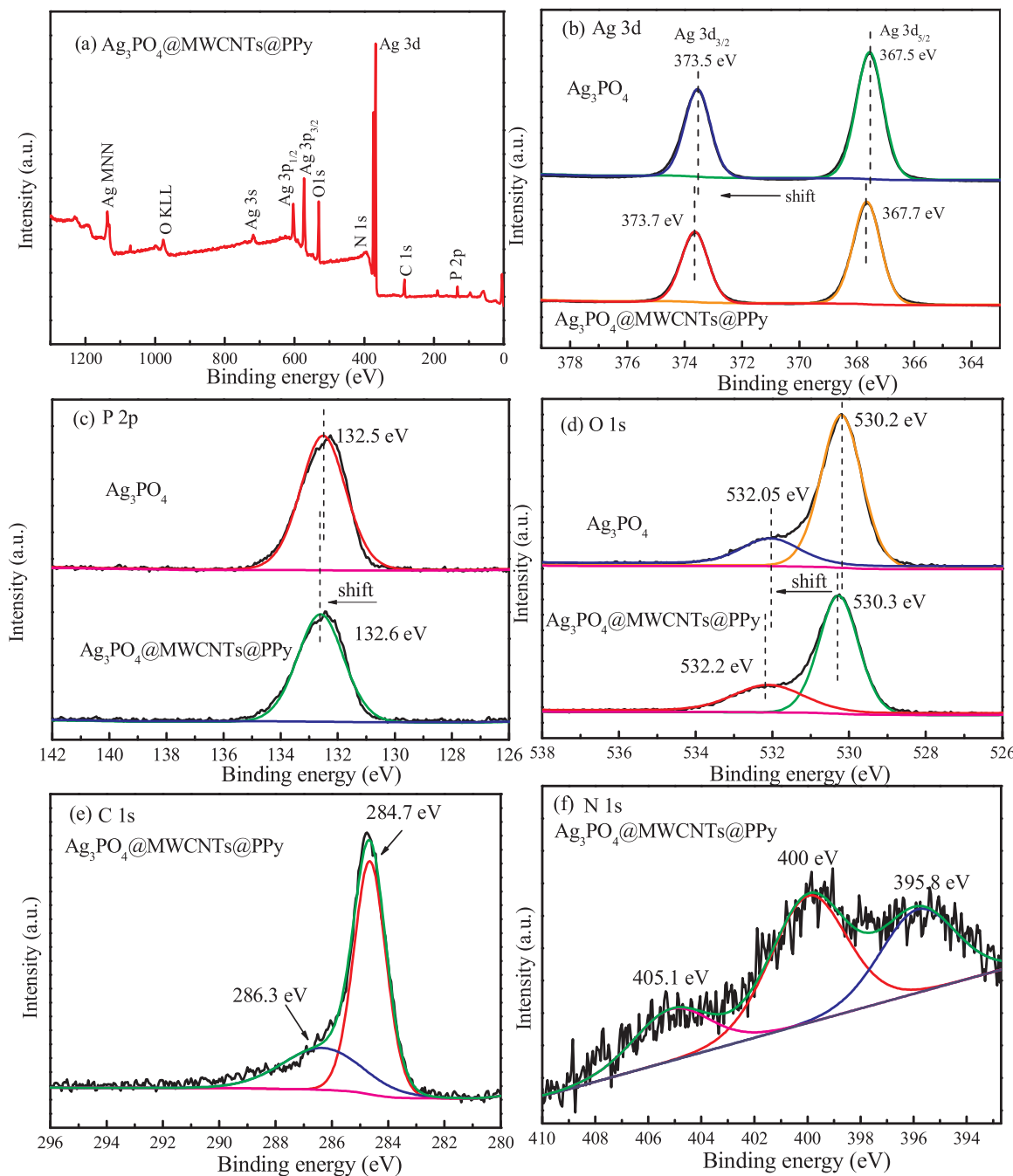


Fig. 5. (a) XPS survey spectra; high resolution XPS spectrum of (b) Ag 3d, (c) P 2p, (d) O 1s, (e) C 1s and (f) N 1s.

two peaks, at BE of 530.3 eV and 532.2 eV, which were corresponded to the bulk lattice O and surface O of Ag_3PO_4 , respectively [33]. Compared with Ag_3PO_4 , the binding energies of Ag, P and O all shifted slightly to positive position in the $\text{Ag}_3\text{PO}_4@\text{MWCNTs}@{\text{PPy}}$ composite (Fig. 5b and c), indicating there was an intense interfacial interaction. Besides, the binding energy was negatively related to surface electron density. Therefore, the above results may imply that the electrons were transferred from Ag_3PO_4 to the surface of MWCNTs and PPy [11,34]. As shown in Fig. 5e, The XPS spectrum of C 1s was deconvoluted into two peaks located at 284.7 eV and 286.3 eV, respectively. The former was mainly attributed to the PPy back bones and sp^2 hybridized carbon, and the peak at 286.3 eV was related to the oxygen bound species C–O and hydroxyl carbon [35,36]. The N 1s spectrum in Fig. 5f could be deconvoluted into three different peaks with binding energies of 395.8 eV, 400 eV and 405.1 eV, representing the strong resonance nitrogen,

amine group and protonated imine group, respectively [36]. The results of XPS further demonstrated the close combination of Ag_3PO_4 , MWCNTs and PPy in $\text{Ag}_3\text{PO}_4@\text{MWCNTs}@{\text{PPy}}$ composite and the intense interfacial interaction among them.

The optical absorption performance of the prepared photocatalysts were characterized by UV-vis diffuse reflectance spectrum (DRS) and presented in Fig. 6a. All photocatalysts presented good optical absorption in the region less than 500 nm. Especially, after coupling with PPy and MWCNTs, the photo-absorption performance of composite catalysts was enhanced obviously in the wavelength range of 500–800 nm. The drastically strengthened photo-absorption of ternary composite indicated that both PPy and MWCNTs was coupled with Ag_3PO_4 successfully, and $\text{Ag}_3\text{PO}_4@\text{MWCNTs}@{\text{PPy}}$ composite could efficiently utilize visible light and obtain more photogenerated electron-hole pairs. In addition, the band gap energy (E_g) of Ag_3PO_4 was

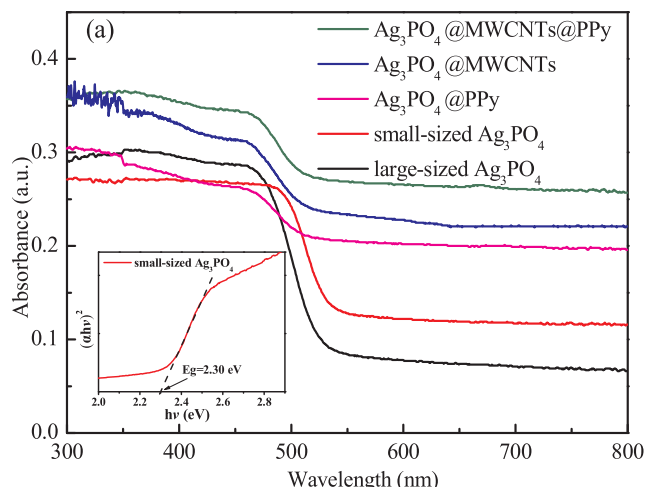


Fig. 6. (a) UV-vis diffuse reflectance spectra of different samples, and the inset image is the band gap energy of small-sized Ag_3PO_4 ; (b) Mott-Schottky plots of Ag_3PO_4 .

calculated by the Kubelka-Munke equation. As presented in the illustration in Fig. 6a, the E_g of small-sized Ag_3PO_4 was estimated to be 2.30 eV. Besides, the flat band potential of Ag_3PO_4 was obtained by Mott-Schottky plot (Fig. 6b) [22,29]. The overall positive slope curve shows that Ag_3PO_4 was the n-type semiconductor. Since the applied potential (E) of Ag_3PO_4 was 0.42 V vs. SCE, the flat band potential was calculated as 0.39 V. It was generally recognized that the conduction band potential (E_{CB}) for n-type semiconductors is more negative by 0.2 V than that of the flat band potential [37]. Thus, the E_{CB} of Ag_3PO_4 was calculated as 0.19 V vs. SCE (equivalent to 0.43 V vs. NHE). Because the E_g of Ag_3PO_4 was 2.3 eV, its valence band potential was determined as 2.73 V vs. NHE. The detailed calculation of E_g and energy band potential was provided in supporting information.

Raman spectroscopy analysis was performed to confirm the interface interaction in the Ag_3PO_4 @MWCNTs@PPy composite. As displayed in Fig. 7, two characteristic peaks centered at 1341 cm^{-1} (D bands) and 1592 cm^{-1} (G bands) were observed in the Raman spectrum of MWCNTs and Ag_3PO_4 @MWCNTs, and the D bands and G bands were corresponded to the amorphous carbon (sp^3) and graphitic carbon (sp^2), respectively. Interestingly, after Ag_3PO_4 coupled with MWCNTs, the I_D/I_G ratio decreased from 1.71 to 1.13, which implied that the sp^3 hybrid carbons were transformed into sp^2 hybrid carbons, and the strong interfacial interaction occurred between Ag_3PO_4 and MWCNTs. In the spectrum of PPy, the peak at 1336 cm^{-1} could be ascribed to the polaron structure in the benzene ring ($\text{C}-\text{N}^+$), and the peak at

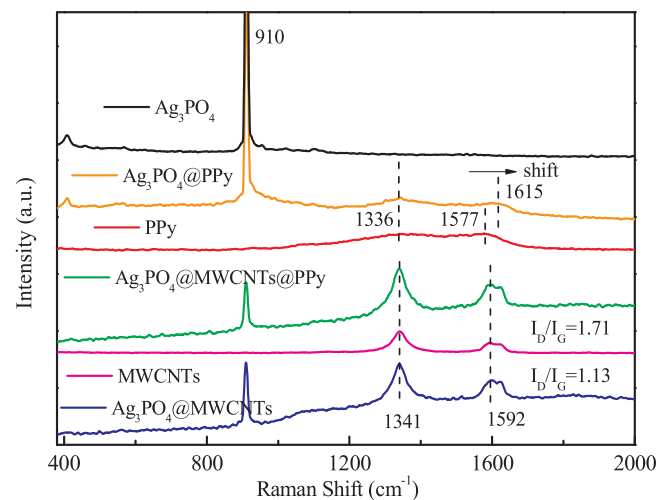


Fig. 7. Raman spectra of different samples.

1577 cm^{-1} was the C=C vibration and vibrational mode of benzenoid unit [22,35,38]. After the incorporation of PPy, the characteristic peaks at 1577 cm^{-1} in the complex samples moved to a higher wavenumber (1615 cm^{-1}), which implied the change of conjugation state and the strengthening bond strengths of C=N (C=C) and C-N. It also indicated an intensive interaction between PPy and Ag_3PO_4 [39,40]. The intense sharp peak at 910 cm^{-1} could be assigned to the motion of terminal oxygen bond vibration of PO_4^{3-} [41]. The above results demonstrated that the coupling among Ag_3PO_4 , PPy and MWCNTs resulted in the strong interfacial interaction among them.

PL spectra and transient photocurrent responses have been widely used to investigate the photogenerated charge separation of photocatalysts [42]. As presented in Fig. 8a, large-sized Ag_3PO_4 exhibited the highest PL intensity, implying high recombination rate of photogenerated electron-hole pairs. In contrast, the small-sized Ag_3PO_4 has lower PL signal, which demonstrated that reducing crystal size of catalyst could effectively prolong carrier lifetime. Compared with the single Ag_3PO_4 , the binary and ternary composite catalysts all displayed considerable decrease in the peak intensity, and the Ag_3PO_4 @MWCNTs@PPy composite displayed the lowest PL intensity, indicating the efficient interfacial electron-hole pairs transfer and excellent separation efficiency. Moreover, the transient photocurrent responses were also carried out to test the photoresponse of different samples. As illustrated in Fig. 8b, quick response could be observed after the working electrode was exposed to the light illumination. The photocurrent densities of binary and ternary catalysts were much higher than those of pure Ag_3PO_4 , and the strongest photocurrent response was achieved in Ag_3PO_4 @MWCNTs@PPy composite, indicating significantly enhanced separation efficiency of carriers on Ag_3PO_4 @MWCNTs@PPy composite. Above results indicated that the separation efficiency of photogenerated electron-hole pairs was remarkably improved after the incorporation of MWCNTs and PPy, which were resulted from the spatial separation of photogenerated carriers on Ag_3PO_4 . The MWCNTs and PPy in Ag_3PO_4 @MWCNTs@PPy composite could be utilized as the conductors of photogenerated electrons and transport materials of photogenerated holes, respectively. The synergies between them promoted the rapid migration and separation of photogenerated charge, which was favorable for achieving enhanced visible light photocatalytic activity. This will be discussed in detail in the mechanism section.

3.2. Photocatalytic performance and mineralization ability

To evaluate the photocatalytic performance of the prepared samples, tetracycline hydrochloride (TC) and phenol, as typical antibiotics

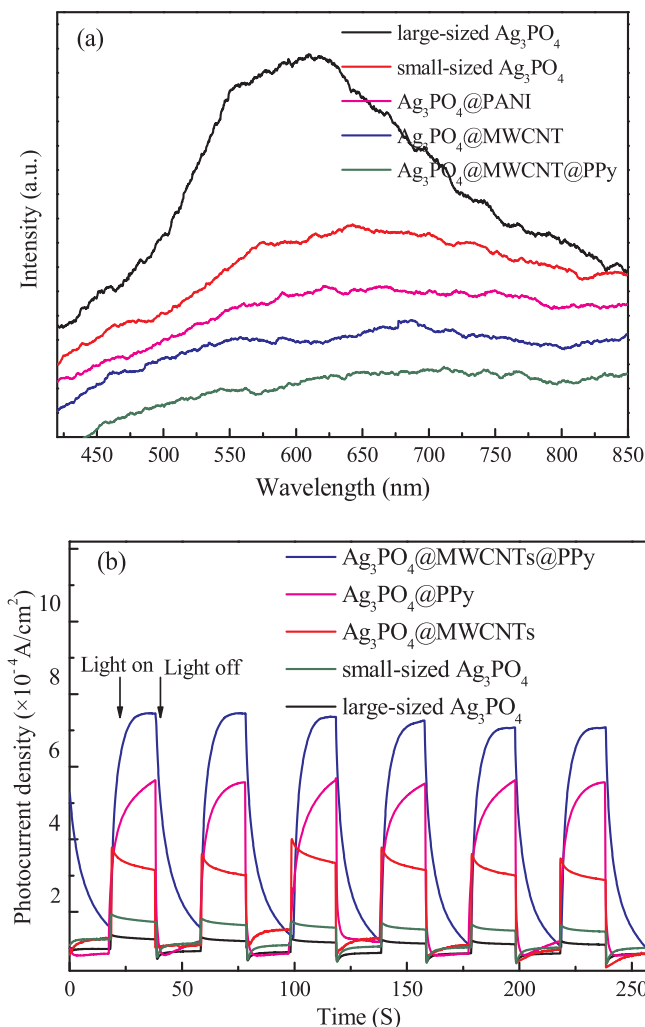


Fig. 8. (a) Photoluminescence (PL) spectra of the prepared samples; (b) photocurrent response density of as-prepared samples.

and phenolic compounds respectively, were selected as model pollutants for degradation experiments. Before light irradiation, 30 min of dark adsorption experiment was carried out to confirm the adsorption-desorption equilibrium. As presented in Fig. 9a, the photocatalytic activity of large-sized Ag_3PO_4 was poor, and its degradation rate for phenol was only 27.88% after 30 min irradiation. However, the removal rate of small-sized Ag_3PO_4 could reach 66.53%, which indicated that reducing the size of Ag_3PO_4 was an effective way to enhance photocatalytic activity. Compared with Ag_3PO_4 , all $\text{Ag}_3\text{PO}_4@\text{MWCNTs}$ composite displayed much higher photocatalytic degradation efficiency. Particularly, the $\text{Ag}_3\text{PO}_4@60$ mL MWCNTs exhibited the highest photocatalytic activity, and 99.03% of phenol could be degraded after 30 min irradiation. To investigate the photocatalytic degradation process and quantify the photocatalytic activity of different catalysts, the pseudo-first-order kinetic model was employed to simulate experimental data, and the results were presented in Fig. 9d. It could be seen that all the photocatalytic process fitted well with the model ($R^2 > 0.99$). The maximum rate constant k (for $\text{Ag}_3\text{PO}_4@60$ mL MWCNTs, 0.127 min^{-1}) was up to 14.1 times as much as the large-sized Ag_3PO_4 (0.009 min^{-1}) and 3.6 times that of small-sized Ag_3PO_4 (0.035 min^{-1}). The results demonstrated that reducing the size of Ag_3PO_4 and introduction of MWCNTs into $\text{Ag}_3\text{PO}_4@\text{MWCNTs}$ composites could significantly improve the catalytic performance and accelerate the photocatalytic degradation rate, which was because the presence of smaller Ag_3PO_4 particles could prolong the lifetime of

photogenerated carriers, and the excellent conductivity of MWCNTs made it a superior acceptor for the photogenerated electrons to suppress the recombination of photogenerated electron-holes pairs. To further improve the photocatalytic performance, PPy was incorporated and coupled with the binary catalyst. As shown in Fig. 9b, only a small amount of phenol was degraded in the presence of PPy. Comparing with Ag_3PO_4 , $\text{Ag}_3\text{PO}_4@\text{PPy}$ and $\text{Ag}_3\text{PO}_4@\text{MWCNTs}$ composite, the ternary $\text{Ag}_3\text{PO}_4@\text{MWCNTs}@PPy$ composite exhibited superior photocatalytic activity, and the $\text{Ag}_3\text{PO}_4@\text{MWCNTs}@3$ mL PPy composite achieved the highest degradation efficiency (100%) in 20 min. The rate constant (k) of phenol degradation by $\text{Ag}_3\text{PO}_4@\text{MWCNTs}@3$ mL PPy was 0.23 min^{-1} , which was about 6.6 times that of pure small-sized Ag_3PO_4 (0.035 min^{-1}), and it was up to 1.7 and 1.8-fold higher than that of $\text{Ag}_3\text{PO}_4@\text{PPy}$ (0.135 min^{-1}) and $\text{Ag}_3\text{PO}_4@\text{MWCNTs}$ (0.126 min^{-1}), respectively (Fig. 9e). Moreover, TC was also used to further assess the photocatalytic activity of the prepared photocatalysts (Fig. 9c and f). Compared with other catalysts, $\text{Ag}_3\text{PO}_4@\text{MWCNTs}@PPy$ composite also exhibited the highest photocatalytic activity and the fastest degradation rate. Especially, it could degrade 98.48% of TC after only 2 min light irradiation, and the TC was completely degraded after 5 min. The above results indicated that the photocatalytic activity of Ag_3PO_4 could be significantly improved by coupling with MWCNTs and PPy.

The mineralization of phenol and TC was also investigated. Fig. 10a depicted the total organic carbon (TOC) removal of phenol by as-prepared photocatalysts [43,44]. Only 20.57% phenol was mineralized by single large-sized Ag_3PO_4 , while the mineralization efficiency reached 50.62%, 71.17%, 73.38% and 80.12% with 30 min irradiation for the single small-sized Ag_3PO_4 , $\text{Ag}_3\text{PO}_4@\text{MWCNTs}$, $\text{Ag}_3\text{PO}_4@\text{PPy}$ and $\text{Ag}_3\text{PO}_4@\text{MWCNTs}@PPy$ composite, respectively. The results demonstrated that $\text{Ag}_3\text{PO}_4@\text{MWCNTs}@PPy$ composite exhibited excellent mineralization ability for phenol degradation. However, all catalysts showed unsatisfactory mineralization efficiency for TC after 20 min illumination (Fig. 10B), and even $\text{Ag}_3\text{PO}_4@\text{MWCNTs}@PPy$ composite only achieved 12.63% TOC removal efficiency. Thus, the TC may only be degraded into intermediates with small molecules. Therefore, the 3D EEMs technology and LC-MS were used to further explore the degradation of TC. As shown in Fig. 10C, samples mappings were collected after adsorption equilibrium in dark and 1, 3, 5, 10, 20 min of light exposure, respectively. As presented in Fig. 10a, there was no signal could be observed, indicating the TC molecule was not decomposed into other products during the adsorption process. However, after one minute of illumination (Fig. 10b), two distinct peaks at 248/497 nm and 341/479 nm ($\lambda_{\text{ex}}/\lambda_{\text{em}}$) appeared, and the intensity of fluorescence signals was 878.0 and 210.7, respectively. According to the previous report, these two peaks were attributed to the fulvic acids- and humic acids-like fluorescence region, respectively. Peak A (fulvic acids-like) appeared at $\lambda_{\text{ex}}/\lambda_{\text{em}}$ (237–260 nm)/(400–500 nm) and peak B (humic acids-like) appeared at $\lambda_{\text{ex}}/\lambda_{\text{em}}$ (300–370 nm)/(400–500 nm) [45,46]. The detailed fluorescence spectra data were provided in Table S2. It could be seen that the intensity of fluorescence signal varied with irradiation time, and the position of the strongest signal peaks was also changing, which indicated that fulvic acids-like or humic-like compounds were degraded and transformed [47,48]. For example, the position of the strongest peak in the fulvic acids-like fluorescence region changed from 248/497 nm to 260/524 nm after 5 min illumination, which also occurred in the humic acids-like fluorescence region when the irradiation time at 10 min.

In order to further investigate the specific degradation intermediates and pathway of TC, the degraded solution samples were analyzed by LC-MS technology [49,50]. The MS spectra of intermediates were presented in Fig. S3. As illustrated in Fig. S3a, the peak located at m/z 445 was identified as TC molecule. The functional groups of TC with relatively high electron density, including double bond, phenolic group and amine group, were easily attacked by radicals in photocatalytic oxidation [51,52]. Among them, double bond was the

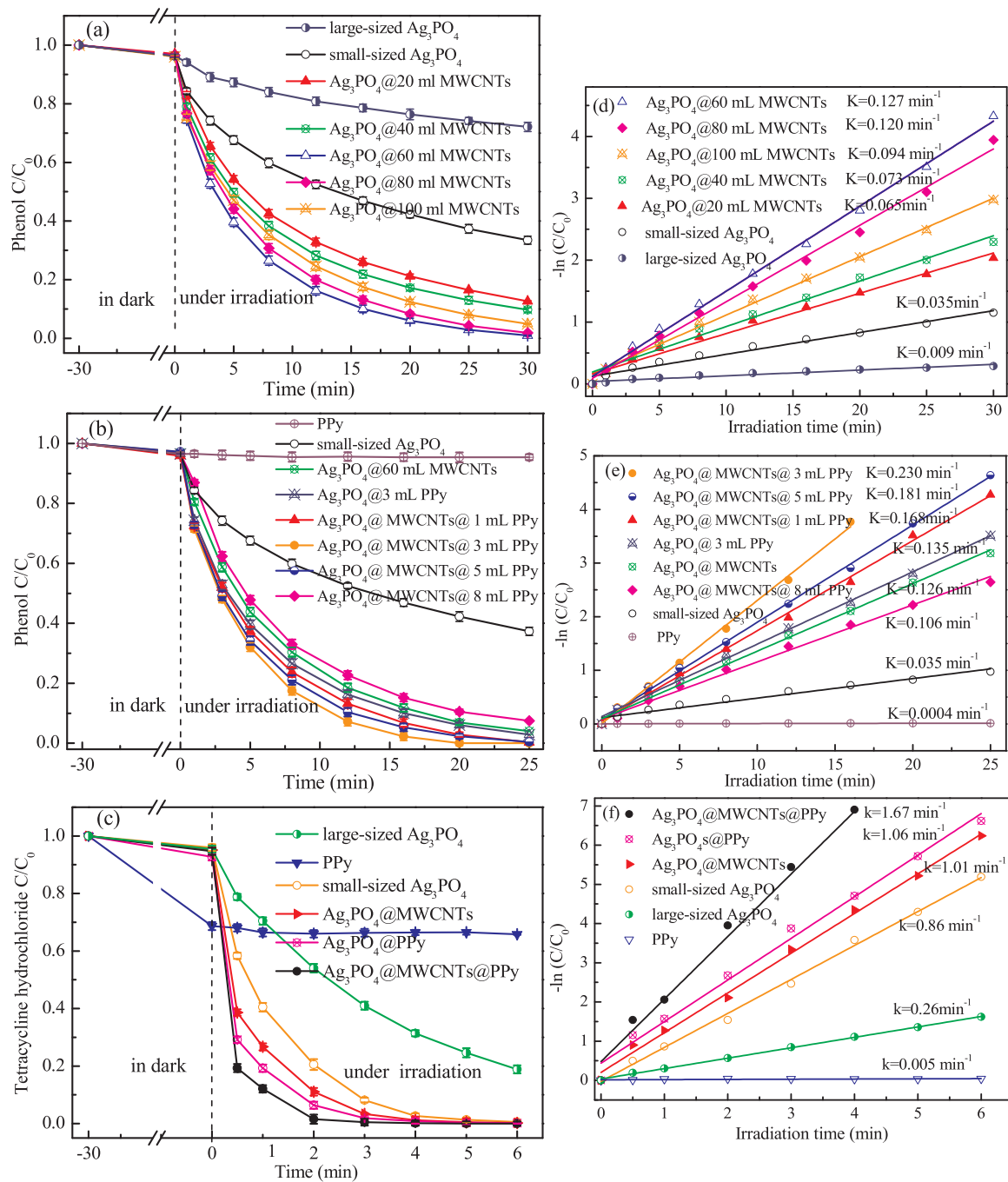


Fig. 9. Photodegradation curves of phenol (a,b) and TC (c) in the presence of as-prepared samples; Reaction kinetic curves (d,e,f) of as-prepared samples corresponding to the photodegradation curves (a,b,c), respectively.

most reactive with radicals [53,54]. Thus the double bond at C2-C3 and C15-C16 position preferentially reacted with radicals and produced the primary intermediate with the *m/z* of 461, which were consistent with the previous study [46,51,55]. Then, it could be attacked by active species at the aromatic ring and further fragmented to the product ion with an *m/z* value of 491 by losing H₂O (Fig. S3d). When radicals reacted with the C12-13 double bond, intermediate (*m/z* = 407) and maleic acid (*m/z* = 116) appeared subsequently (Fig. S3e). Afterwards, by radicals oxidation the -N(CH₃)₂ at position C4, amide group at C2 and -CH₃ at position C8, the intermediate products with *m/z* values of 378, 362, 396, and 351 could be obtained respectively (Fig. S3f, g, h). Finally, these intermediates could be further oxidized into short-chain carboxylic acids by radicals, and the small molecules organic acids with

m/z values of 205, 159, 116, 99 and 72 were detected (Fig. S3i, j, k, l). Based on the above results, a possible photocatalytic degradation pathway of TC was speculated and provided in Fig. 11.

3.3. Photostability and recyclability

To evaluate the photostability and repeatability of as-prepared samples, the recycling experiment for photocatalytic degradation of phenol was carried out, and the results were shown in Fig. 12. A remarkable decrease of photocatalytic performance for pure Ag₃PO₄ could be observed in Fig. 12a. There was about 42.7% reduction in the removal efficiency towards phenol decomposition over pure Ag₃PO₄, while the photocatalytic activity of Ag₃PO₄@MWCNTs@PPy composite

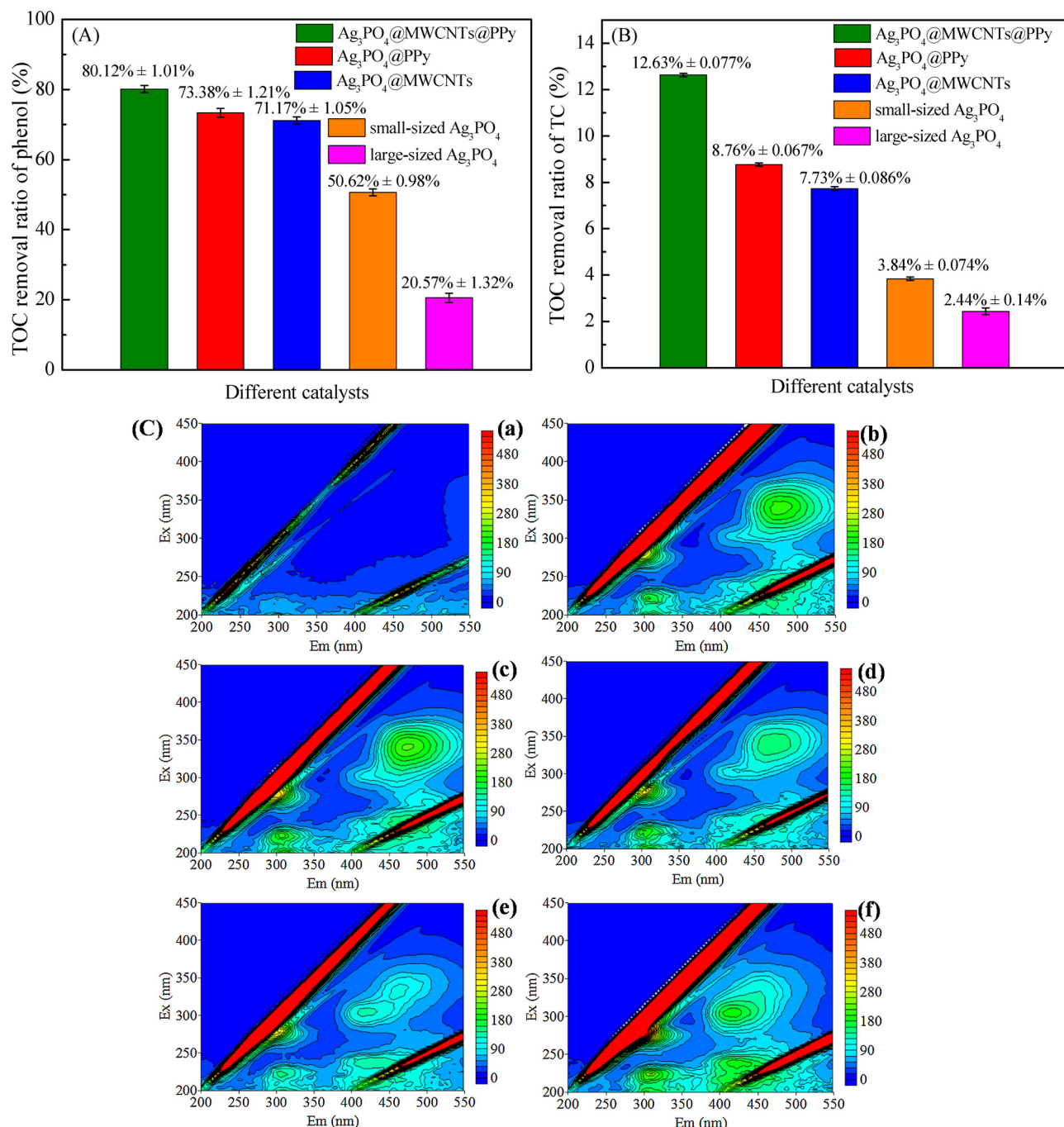


Fig. 10. TOC removal of phenol (A) and TC (B) over various photocatalysts under visible light irradiation for 30 min and 20 min, respectively; (C) 3D EEMs of the TC: (a) collected after 30 min adsorption in dark and (b–f) obtained after an irradiation time of 1, 3, 5, 10 and 20 min, respectively.

did not decline after three consecutive cycles, and 100% of phenol degradation efficiency was still achieved. In addition, the degradation efficiency could still reach 95.6% after four runs, and 87.8% phenol was degraded by $\text{Ag}_3\text{PO}_4@\text{MWCNTs@PPy}$ catalyst after five cycles. The results indicated that the anti-photocorrosion performance of composite photocatalyst was greatly improved after coupling Ag_3PO_4 with MWCNTs and PPy. Moreover, there was also a relatively little loss (approximately 21.4% and 21.1%) in the photocatalytic activity after 5 cycles over $\text{Ag}_3\text{PO}_4@\text{MWCNTs}$ and $\text{Ag}_3\text{PO}_4@\text{PPy}$ composite. The results indicated that the addition of PPy and MWCNTs could significantly enhance both the photocatalytic activity and photostability of Ag_3PO_4 . The significant decrease in photocatalytic activity of Ag_3PO_4 was due to the partial reduction of Ag_3PO_4 into Ag^0 by photoproduced

electrons. However, the conductive MWCNTs that introduced in the composite could serve as an effective acceptor of the photogenerated electrons, hence, the photogenerated electrons of Ag_3PO_4 would be transferred to MWCNTs and not accumulated on the surface of Ag_3PO_4 . Meanwhile, the hybridized PPy could be utilized as the capture trap of photoproduced holes. The system of photogenerated carrier spatial separation was thus constructed, which could promote the rapid separation of electron-hole pairs significantly as well as improve the photoactivity and photostability of catalyst dramatically.

Moreover, in order to further compare and demonstrated the stability of Ag_3PO_4 and $\text{Ag}_3\text{PO}_4@\text{MWCNTs@PPy}$ composite, the XRD patterns of the fresh and used photocatalysts were provided in Fig. 12b. And the XRD spectra were normalized to facilitate peak strength

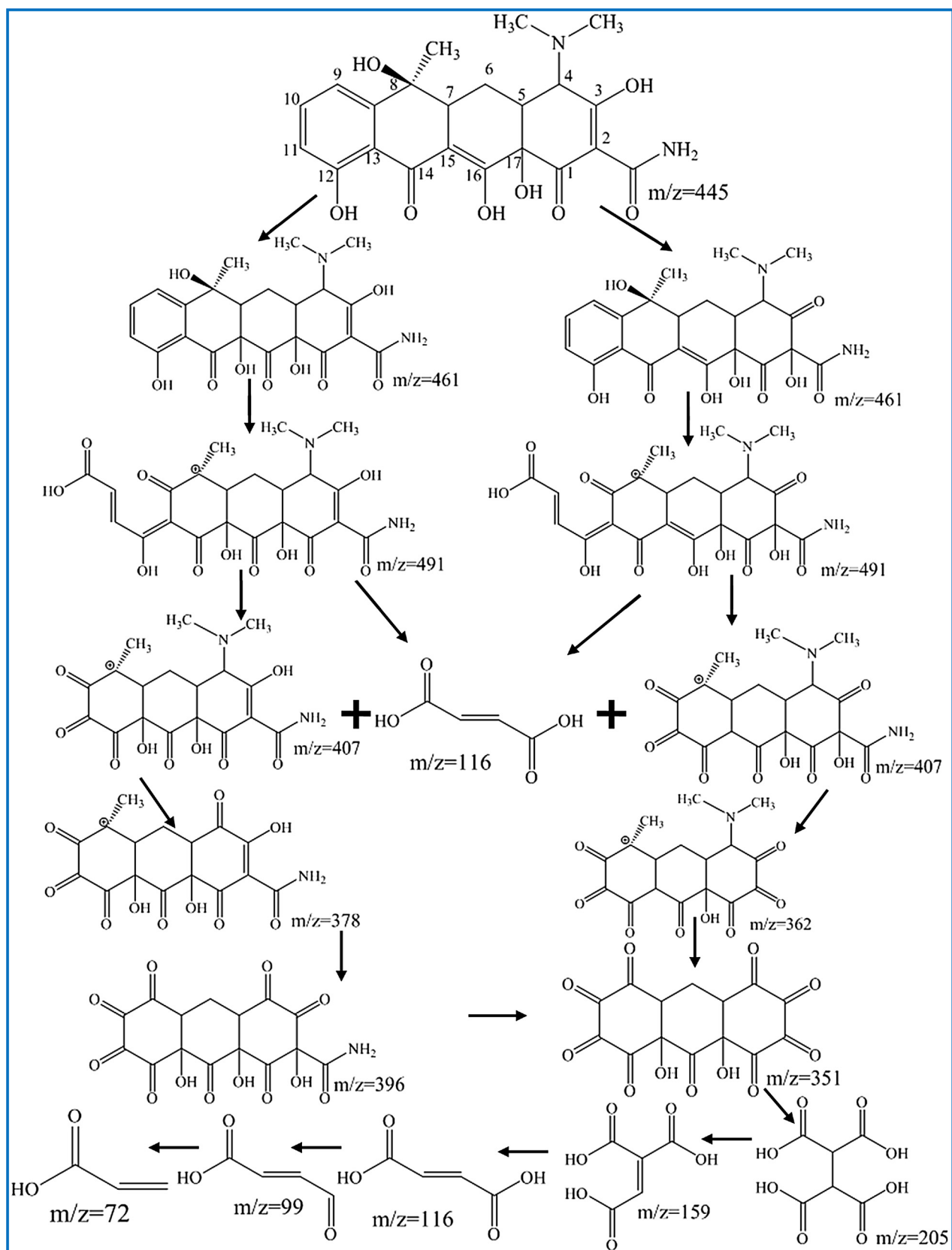


Fig. 11. A possible photocatalytic degradation pathway of TC.

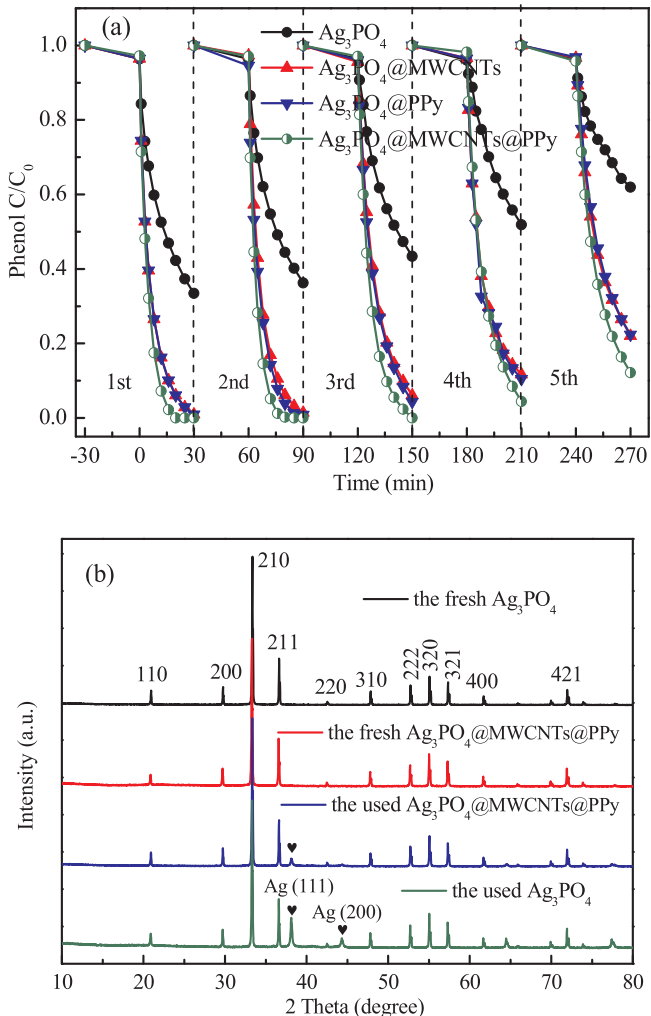


Fig. 12. Cycling test for the photocatalytic degradation of phenol in the presence of different as-prepared samples (a); XRD patterns of the fresh and used photocatalysts (b).

comparison. The obvious characteristic diffraction peaks ascribed to metallic Ag were observed on the XRD pattern of the used Ag_3PO_4 sample, in which the diffraction peaks at 38.12° and 44.28° could be indexed to the (111) and (200) plane for metallic Ag, respectively. The results indicated that a certain amount of Ag_3PO_4 have been converted to metallic Ag after irradiation reaction, and excessive encapsulated metallic Ag affected the light absorption efficiency of Ag_3PO_4 , which could reduce the photocatalytic activity and stability of pure Ag_3PO_4 . In contrast, just a weak diffraction peak at 38.12° was observed on the XRD pattern of the $\text{Ag}_3\text{PO}_4@\text{MWCNTs@PPy}$ composite collected after reaction, suggesting that only a small amount of Ag appeared during the photodegradation process. It was reported that the existence of minor amount of Ag will not reduce the photocatalytic performance, but instead it may act as the charge transmission-bridge to promote the migration of photogenerated electrons and improve the separation efficiency of electron-hole pairs [22,56–58]. The excellent photocatalytic activity and repeatability of $\text{Ag}_3\text{PO}_4@\text{MWCNTs@PPy}$ composite in this study have also proved this point.

3.4. Possible photocatalytic mechanism of $\text{Ag}_3\text{PO}_4@\text{MWCNTs@PPy}$

3.4.1. Active species in reaction system

To investigate the dominant active species produced in the reaction system of $\text{Ag}_3\text{PO}_4@\text{MWCNTs@PPy}$, the trapping experiments were carried out. The Isopropanol (IPA), benzoquinone (BQ), AgNO_3 and

Ethylenediaminetetraacetic acid disodium salt (EDTA-2Na) were utilized as the scavengers for hydroxyl radical ($\cdot\text{OH}$) ($\cdot\text{O}_2^-$), superoxide radical species, photogenerated electron (e^-) and hole (h^+), respectively [59,60]. The degradation curves of phenol over $\text{Ag}_3\text{PO}_4@\text{MWCNTs@PPy}$ with the addition of different scavengers were presented in Fig. 13A. Obviously, the photocatalytic activity of $\text{Ag}_3\text{PO}_4@\text{MWCNTs@PPy}$ almost deactivated in the presence of EDTA-2Na, indicating the holes were the dominant active species in the reaction process. Severe inhibition of photocatalytic activity also occurred with the addition of BQ, which demonstrated that $\cdot\text{O}_2^-$ also played a vital role in the degradation of pollutants. The photocatalytic efficiency decreased after the AgNO_3 and IPA was added respectively, indicating that the role of electrons and $\cdot\text{OH}$ also could not be completely ignored. The results suggested that $\cdot\text{O}_2^-$, e^- , h^+ and $\cdot\text{OH}$ all worked during the photocatalytic degradation procedure, while the predominant active species for the $\text{Ag}_3\text{PO}_4@\text{MWCNTs@PPy}$ should be h^+ and $\cdot\text{O}_2^-$.

In order to further validate and compare the radical generation in the photocatalytic system of Ag_3PO_4 and $\text{Ag}_3\text{PO}_4@\text{MWCNTs@PPy}$, the ESR measurements was also performed. As shown in Fig. 13a and b, under identical irradiation conditions, the characteristic signals of $\cdot\text{O}_2^-$ and $\cdot\text{OH}$ could be clearly observed for both the small-sized Ag_3PO_4 and $\text{Ag}_3\text{PO}_4@\text{MWCNTs@PPy}$ samples, and the peak intensity of ternary composite was much higher than that of small-sized Ag_3PO_4 , indicating the significantly enhanced $\cdot\text{O}_2^-$ and $\cdot\text{OH}$ generation ability of $\text{Ag}_3\text{PO}_4@\text{MWCNTs@PPy}$ composite. The results indicated that coupling with MWCNTs and PPy was beneficial to the formation of more active radicals, which was essential to improve the photocatalytic activity. However, only weak radical signals could be detected in the system of large-sized Ag_3PO_4 , which was because longer time was needed for electrons and holes to diffuse from the photocatalyst bulk phase to the surface in the large-sized particles, resulting in more photogenerated carrier recombination. Meanwhile, it also demonstrated that the new synthesis method of pure Ag_3PO_4 proposed in this study was feasible and effective. Besides, the DMPO- $\cdot\text{O}_2^-$ and DMPO- $\cdot\text{OH}$ signals could not be detected in darkness, demonstrating all radicals were produced in photocatalytic reaction. Moreover, ESR tests with different exposure time were also carried out, and the results were provided in Figs. 13c, d and S4. Obviously, the signal intensities of DMPO- $\cdot\text{O}_2^-$ and DMPO- $\cdot\text{OH}$ significantly increased with exposure time in the system of $\text{Ag}_3\text{PO}_4@\text{MWCNTs@PPy}$ composite, while there was almost no trend of signal enhancement in the system of single Ag_3PO_4 . The results implied that the addition of MWCNTs and PPy made the $\text{Ag}_3\text{PO}_4@\text{MWCNTs@PPy}$ composite possess the ability to produce active radicals continuously, which could be attributed to the excellent carrier separation ability in the ternary system.

3.4.2. Density-function-theory (DFT) calculations

The DFT calculation was performed to further illustrate the photogenerated carrier migration mechanism. The MWCNTs@ $\text{Ag}_3\text{PO}_4@\text{PPy}$ model was constructed and the electronic structures were also analyzed in detail. The density of states (DOS) and the band charge density distributions of MWCNTs@ $\text{Ag}_3\text{PO}_4@\text{PPy}$ model were shown in Fig. 14a. Obviously, there was a small highest occupied energy band (HOEB) around the fermi energy level which was distributed around on the PPy, and it could be regarded as the large conjugated π -orbital. Similarly, the sub-tier HOEB (HOEB-1) at the -0.5 eV energy level was also distributed around on the PPy. Until the energy level decreased to around -0.85 eV, the electrons begin to occupy the Ag_3PO_4 energy band which was consisted by the O 2p orbital (HOEB-2). While for the lowest unoccupied energy band (LUEB), it was mainly composed of the Ag 4d orbital in Ag_3PO_4 crystal with the small C 2p orbital in CNTs. Increasing the energy level to around 0.8 eV, the second LUEB (LUEB + 1) was similar to LUEB but with more C 2p orbital on CNTs. Therefore, when this MWCNTs@ $\text{Ag}_3\text{PO}_4@\text{PPy}$ material was exposed to visible light, there were two possible excitation processes: (i) the electrons on PPy are excited to Ag_3PO_4 : HOEB/HOEB-1 \rightarrow LUEB/LUEB + 1, and (ii) the

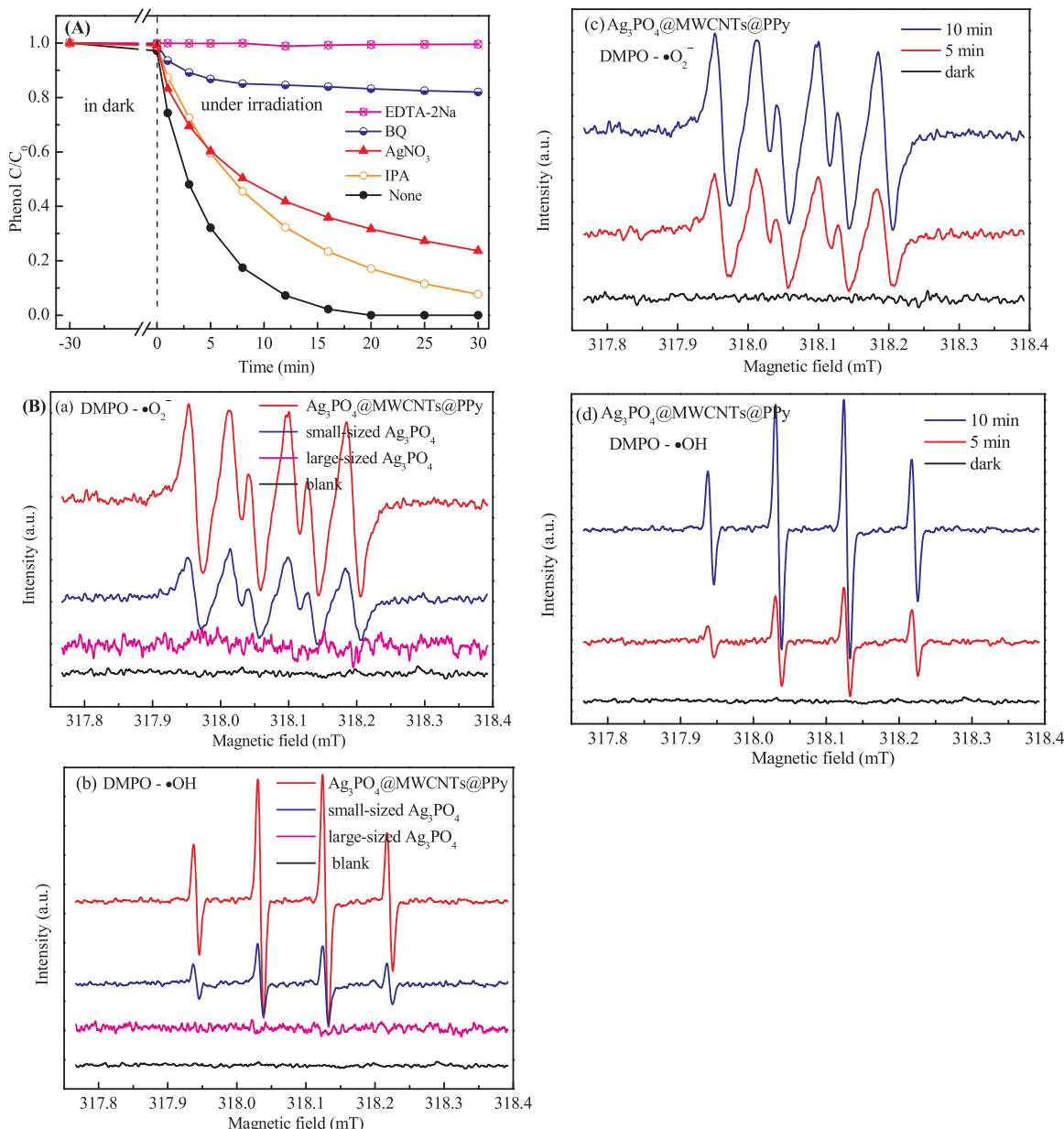


Fig. 13. (A) Photodegradation curves of phenol over Ag_3PO_4 @MWCNTs@PPy composite with different active species scavengers under visible light irradiation. (B) ESR spectra of radical adducts trapped by DMPO in the different samples dispersion under both the dark and visible light irradiation ($\lambda > 420 \text{ nm}$) condition: (a,c) in methanol dispersion for DMPO-•O₂⁻; (b,d) in aqueous dispersion for DMPO-•OH.

electrons on Ag_3PO_4 are excited to Ag_3PO_4 : HOEB-2 → LUEB/LUEB + 1. It was impossible to directly excite the electrons from HOEB/HOEB-1 to LUEB/LUEB + 1 due to the space separation, the excitation process (i) was thus ruled out. Therefore, only the electrons on HOEB-2 could be excited to LUEB/LUEB + 1. The excitation of electrons leaves behind the photogenerated holes at HOEB-2, electrons at high energy levels energy bands (HOEB/HOEB-1) prefer to spontaneously migrate to low energy level HOEB-2, leading to the migration of photogenerated holes from HOEB-2 (Ag_3PO_4) to HOEB/HOEB-1 (PPy). Some excited electrons in Ag 3d orbitals will recombine with photogenerated holes, while a large number of excited electrons in C 2p orbitals would be transferred to the surface of catalyst through MWCNTs. Finally, the excited electrons and photogenerated holes of Ag_3PO_4 were enriched on MWCNTs and PPy, respectively (Fig. 14b).

Planar averaged self-consistent electrostatic potential as a function of position in the Z-direction for MWCNTs@ Ag_3PO_4 @PPy model was displayed in Fig. 14c. The electrostatic potential of Ag_3PO_4 was lower

than that of MWCNTs and PPy. The higher potential near MWCNTs leads to potential well at the interface between MWCNTs and Ag_3PO_4 . Similarly, it could also be found in the interface between Ag_3PO_4 and PPy. The appearance of such a built-in potential well could drive efficient charge separation in the composites, and effectively hinder the recombination of photogenerated carriers in Ag_3PO_4 @MWCNTs@PPy composite [61]. Moreover, to explore the influence of the addition of MWCNTs and PPy on the light absorption of composite catalyst, the imaginary part of the dielectric function and the UV-vis absorption spectra of pure Ag_3PO_4 , PPy and Ag_3PO_4 @MWCNTs@PPy were examined, and the results were shown in Fig. 14d. The absorption intensity of Ag_3PO_4 and PPy was weak in the visible-light region, while the Ag_3PO_4 @MWCNTs@PPy composite exhibited the strong visible-light adsorption at 380–600 nm. This was consistent with the results of DRS. Therefore, it was reasonable to conclude that Ag_3PO_4 @MWCNTs@PPy composite would lead to strong absorption in the UV-vis region, which is one of the most important factors to improving

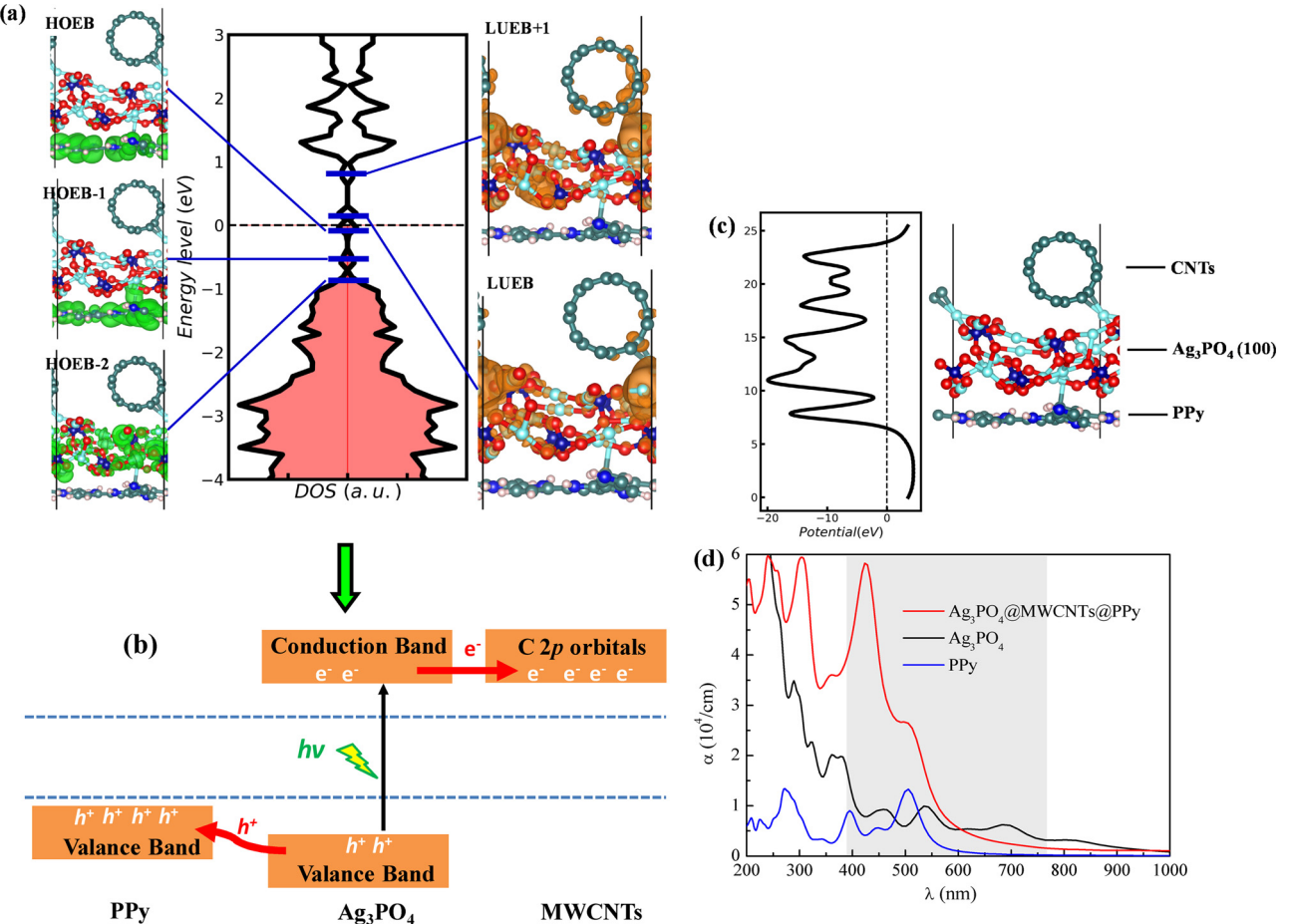


Fig. 14. The density of states (DOS) of the CNTs@Ag₃PO₄@PPy model with the band decomposed charge density of HOEB-2, HOEB-1, HOEB, LUEB and LUEB + 1 bands. The green and orange colors represent the charge density distribution with and without electron occupation, respectively. 3D charge density difference with an isovalue of 0.0007 e⁻/Å³(a); Sketch map of photo-generated carriers migration mechanism over Ag₃PO₄@MWCNTs@PPy (b); Planar averaged self-consistent electrostatic potential as a function of position in the Z-direction for Ag₃PO₄@MWCNTs@PPy model (c); Optical absorption coefficient (α) for pure Ag₃PO₄ bulk, PPy and Ag₃PO₄@MWCNTs@PPy composite (d). (For interpretation of the references to colour in this figure legend, the reader is referred to the web version of this article).

the photocatalytic activity of Ag₃PO₄.

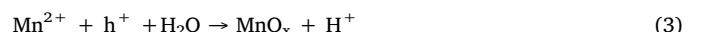
3.4.3. Photo-deposition of platinum and manganese oxide

On the basis of the above theoretical calculations, photochemical deposition experiments were carried out to further verify the migration direction of photogenerated electrons and holes. The photo-deposition of Pt on the surface of Ag₃PO₄@MWCNTs was carried out using H₂PtCl₆·6H₂O as precursors and water as the holes scavenger [17,18,20]. SEM image (Fig. 15a) clearly showed that the particles of Pt were deposited on the MWCNTs. To obtain the detailed information, the TEM-EDS and HRTEM images of the sample was recorded. As presented in Fig. 15c and d, there were many nanoparticles adhered to the surface of MWCNTs. The clear lattice fringes could be observed obviously, and the fringes with lattice spacing of 0.226 nm could be indexed to the (111) planes of face-centered cubic Pt, in good agreement with the JCPDS card No. 04-0802. The TEM-EDS spectra in Fig. 15b also proved the existence of Pt, as for the presence of C and Cu, it was due to the use of carbon film and copper mesh in the sample determination process. Decrease of the metal valence in metal ion precursors indicated that the metal ions were photoreduced on the surface of MWCNTs [17]. Namely, the photogenerated electrons of Ag₃PO₄ were readily transferred to MWCNTs and available for the reduction reaction.

The photoreduction of Pt ions could be described as follows:



Moreover, photooxidation depositions of Mn²⁺ ions on Ag₃PO₄@PPy were carried out with IO₃⁻ as electron acceptors [20]. Manganese oxides could be found deposited on PPy surface (Fig. 15e). To further prove the existence of manganese oxide, the EDS-mapping analysis of the sample were provided in Fig. 15f-h. As shown in Fig. 15g and h, the dense regions of P and N elements represented the Ag₃PO₄ and PPy, respectively. It could be clearly seen that Mn and O elements were uniformly distributed on the surface of PPy, suggesting the formation of MnO_x (Fig. 15i and j). The appearance of manganese oxides indicated that photo-oxidation took place on PPy, that is, the photogenerated holes of Ag₃PO₄ tended to migrate to the surface of PPy. The reactions could be described as follows:



3.4.4. Spatial separation system of photogenerated carriers on Ag₃PO₄@MWCNTs@PPy

The above DFT calculation and experimental data fully proved that a photogenerated carriers spatial separation system has been constructed in Ag₃PO₄@MWCNTs@PPy composite. According to the

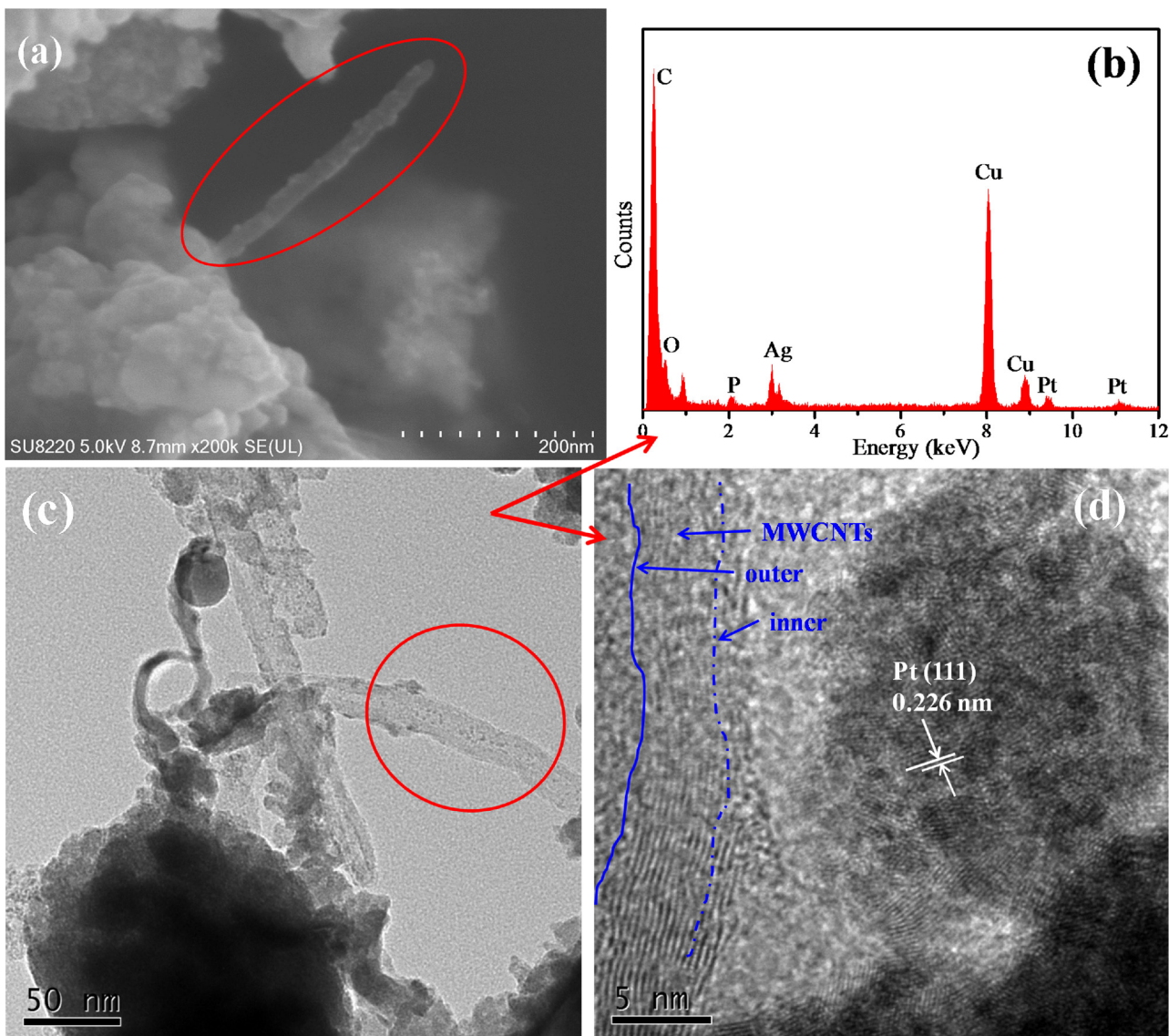


Fig. 15. The SEM images (a), TEM-EDS (b) and HRTEM images analysis (c, d) of Ag_3PO_4 @MWCNTs composite with photo-deposition of Pt; SEM images and SEM-EDS elemental mapping images of Ag_3PO_4 @PPy composite with photo-deposition of MnO_x .

above-mentioned information, the CB potential and VB potential of Ag_3PO_4 were calculated to be 0.43 eV and 2.73 eV, respectively. The LUMO and HOMO potentials of PPy were -0.1 and 2.1 eV, respectively (Fig. S5). Hence, under visible light irradiation, both Ag_3PO_4 and PPy could be excited to produce excited electrons and photogenerated holes, respectively. Since MWCNTs possess high conductivity for charge transport, they could be used as excellent candidates for improving charge extraction and transport in photocatalysis [12,62,63]. PPy is a kind of π -conjugated conductive polymers with excellent conductivity, which could be utilized as a good material for transporting holes [23,24,64]. The results of photochemical deposition experiments also demonstrated that MWCNTs and PPy could be used as good acceptors and conductors of photogenerated electrons and photogenerated holes, respectively. In summary, the separation and migration paths of photogenerated carriers could be simply summarized as follows (Fig. S6):

Under visible light irradiation, the electrons at the VB of Ag_3PO_4 were easily excited to the CB, inducing the formation of holes in the VB. Similarly, this process occurred on PPy. The excited state electrons at high energy bands in PPy could readily inject into CB of Ag_3PO_4 , and the photogenerated holes will migrate from Ag_3PO_4 to PPy. Because of the coupling of Ag_3PO_4 with MWCNTs, the photogenerated electrons on

Ag_3PO_4 tended to accumulate on MWCNTs and transferred to the surface of catalyst, and then reacted with oxygen and water to yield superoxide and hydroxyl radicals, which could attack and degrade pollutant molecules. Meanwhile, the photogenerated holes were transferred to the surface of the catalyst through PPy, and the photogenerated holes had a strong affinity to capture electrons from adsorbed pollutant molecules, and consequently oxidize and degrade pollutants. These were also in line with the results of ESR and radical trapping experiments, that is, the photogenerated holes played a crucial role in the degradation of pollutants. In this way, the spatial separation system of photogenerated carriers was successfully constructed in the Ag_3PO_4 @MWCNTs@PPy composite, which greatly improved the charge separation efficiency and photocatalytic performance of catalyst.

4. Conclusions

In summary, a new method of preparing Ag_3PO_4 with uniform small-sized particles was proposed, in which the large Ag_3PO_4 polyhedron crystals with a diameter of 10–25 μm were transformed into particles ranged from 0.2 to 1.4 μm in diameter. A novel photocatalyst

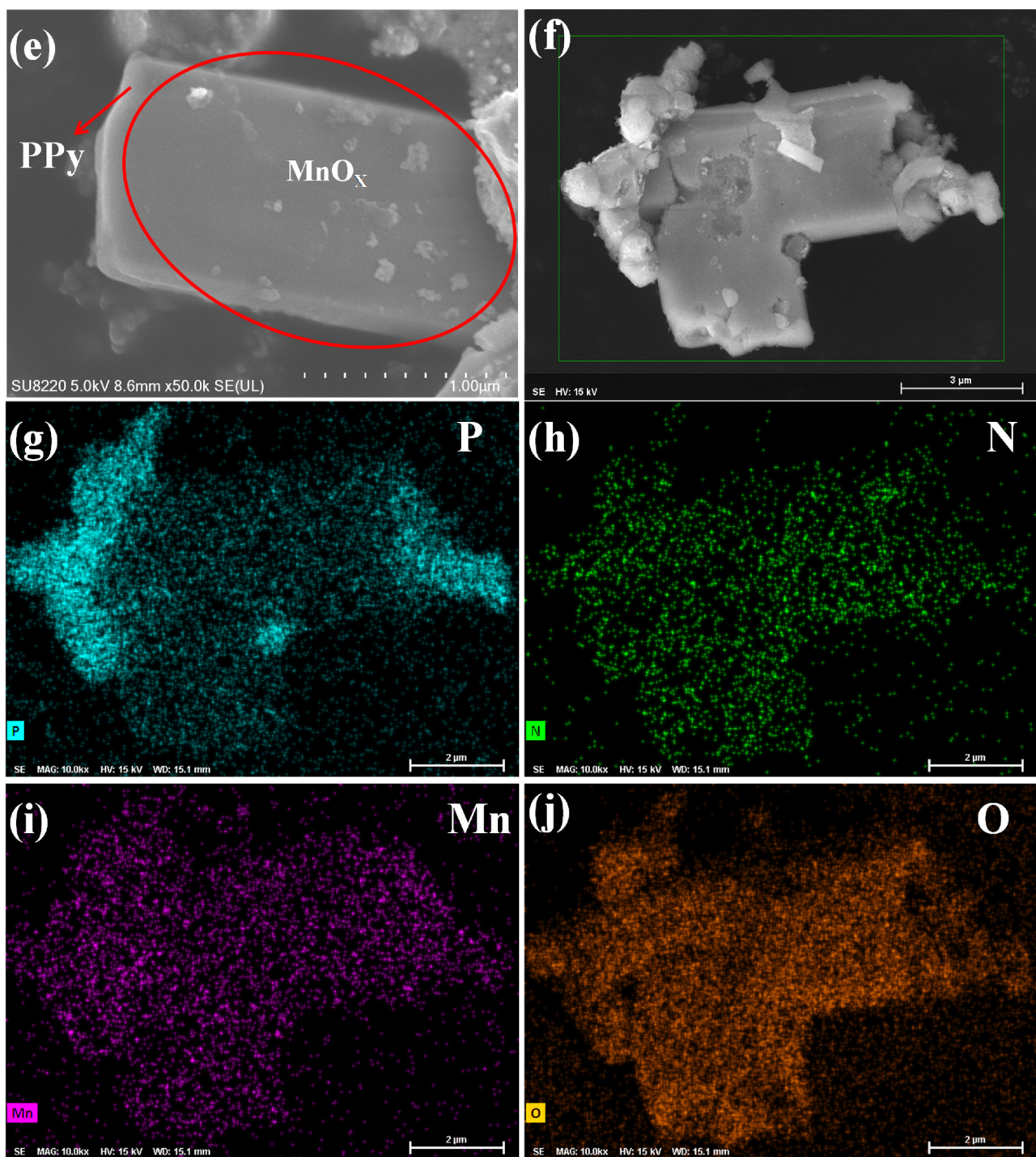


Fig. 15. (continued)

Ag_3PO_4 @MWCNTs@PPy was prepared for the first time. The results of DFT calculation and photochemical deposition experiments indicated that a spatial separation system of photogenerated carriers in Ag_3PO_4 @MWCNTs@PPy composite was successfully constructed, thus, high separation efficiency of electron-hole pairs and excellent photocatalytic performance were achieved. The ternary catalyst exhibited superior photocatalytic activities, excellent mineralization ability and great stability under visible light irradiation. 80.12% of phenol could be mineralized within 20 min, and TC was mainly degraded into small molecule acids, fulvic acids- and humic acids-like matters. This work provided an efficient photocatalytic material for environmental remediation. The strategy for constructing the carrier spatial separation

system is promising for designing high efficient solar energy conversion photocatalysts.

Declaration of Interest Statement

The authors declare that they have no known competing financial interests or personal relationships that could have appeared to influence the work reported in this paper.

Acknowledgments

This work was supported by the project of National Natural Science

Foundation of China (Grant No.: 51478172 and 51521006), the Department of Science and Technology of Guangdong Province of China (Contract No.: 2018S0011), the International S&T Cooperation Program of China (Contract No.: 2015DFG92750) and the Department of Science and Technology of Hunan Province of China (Contract No.: 2017JJ2029 and 2017SK2362).

Appendix A. Supplementary data

Supplementary material related to this article can be found, in the online version, at doi:<https://doi.org/10.1016/j.apcatb.2019.117969>.

References

- [1] A. Trowbridge, D. Reich, M.J. Gaunt, Multicomponent synthesis of tertiary alkylamines by photocatalytic olefin-hydroaminoalkylation, *Nature* 561 (2018) 522–527.
- [2] D. Liu, J. Wang, X.J. Bai, R.L. Zong, Y.F. Zhu, Self-assembled PDINH supramolecular system for photocatalysis under visible light, *Adv. Mater.* 28 (2016) 7284–7290.
- [3] H. Yamashita, K. Mori, Y. Kuwahara, T. Kamegawa, M. Wen, P. Verma, M. Che, Single-site and nano-confined photocatalysts designed in porous materials for environmental uses and solar fuels, *Chem. Soc. Rev.* 47 (2018) 8072–8096.
- [4] L.J. Xu, J.L. Wang, Magnetic nanoscaled $\text{Fe}_3\text{O}_4/\text{CeO}_2$ composite as an efficient Fenton-like heterogeneous catalyst for degradation of 4-chlorophenol, *Environ. Sci. Technol.* 46 (2012) 10145–10153.
- [5] H. Park, H.-i. Kim, G.-h. Moon, W. Choi, Photoinduced charge transfer processes in solar photocatalysis based on modified TiO_2 , *Energy Environ. Sci.* 9 (2016) 411–433.
- [6] W.J. Wang, T.C. An, G.Y. Li, Y.C. Li, J.C. Yu, P.K. Wong, Free-standing red phosphorous/silver sponge monolith as an efficient and easily recyclable macroscale photocatalyst for organic pollutant degradation under visible light irradiation, *J. Colloid Interface Sci.* 518 (2018) 130–139.
- [7] J.L. Wang, S.Z. Wang, Activation of persulfate (PS) and peroxymonosulfate (PMS) and application for the degradation of emerging contaminants, *Chem. Eng. J.* 334 (2018) 1502–1517.
- [8] X.F. Yang, H.Y. Cui, Y. Li, J.L. Qin, R.X. Zhang, H. Tang, Fabrication of Ag_3PO_4 -graphene composites with highly efficient and stable visible light photocatalytic performance, *ACS Catal.* 3 (2013) 363–369.
- [9] Y.P. Bi, S.X. Ouyang, N. Umezawa, J.Y. Cao, J.H. Ye, Facet effect of single-crystalline Ag_3PO_4 sub-microcrystals on photocatalytic properties, *J. Am. Chem. Soc.* 133 (2011) 6490–6492.
- [10] H.C. Zhang, H. Huang, H. Ming, H.T. Li, L.L. Zhang, Y. Liu, Z.H. Kang, Carbon quantum dots/ Ag_3PO_4 complex photocatalysts with enhanced photocatalytic activity and stability under visible light, *J. Mater. Chem.* 22 (2012) 10501–10506.
- [11] T. Cai, L.L. Wang, Y.T. Liu, S.Q. Zhang, W.Y. Dong, H. Chen, X.Y. Yi, J.L. Yuan, X.N. Xia, C.B. Liu, S.L. Luo, $\text{Ag}_3\text{PO}_4/\text{Ti}_3\text{C}_2$ MXene interface materials as a Schottky catalyst with enhanced photocatalytic activities and anti-photocorrosion performance, *Appl. Catal. B: Environ.* 239 (2018) 545–554.
- [12] D.J. Martin, G.G. Liu, S.J. Moniz, Y.P. Bi, A.M. Beale, J.H. Ye, J.W. Tang, Efficient visible driven photocatalyst, silver phosphate: performance, understanding and perspective, *Chem. Soc. Rev.* 44 (2015) 7808–7828.
- [13] G. Botelho, J. Andres, L. Gracia, L.S. Matos, E. Longo, Photoluminescence and photocatalytic properties of Ag_3PO_4 microcrystals: an experimental and theoretical investigation, *ChemPlusChem* 81 (2016) 202–212.
- [14] J.K. Liu, C.X. Luo, J.D. Wang, X.H. Yang, X.H. Zhong, Controlled synthesis of silver phosphate crystals with high photocatalytic activity and bacteriostatic activity, *CrystEngComm* 14 (2012) 8714–8721.
- [15] C.T. Dinh, T.D. Nguyen, F. Kleitz, T.O. Do, Large-scale synthesis of uniform silver orthophosphate colloidal nanocrystals exhibiting high visible light photocatalytic activity, *Chem. Commun.* 47 (2011) 7797–7799.
- [16] P.Y. Dong, Y.H. Wang, H.H. Li, H. Li, X.L. Ma, L.L. Han, Shape-controllable synthesis and morphology-dependent photocatalytic properties of Ag_3PO_4 crystals, *J. Mater. Chem. A* 1 (2013) 4651–4656.
- [17] R.G. Li, F.X. Zhang, D. Wang, J.X. Yang, M.R. Li, J. Zhu, X. Zhou, H.X. Han, C. Li, Spatial separation of photogenerated electrons and holes among {010} and {110} crystal facets of BiVO_4 , *Nat. Commun.* 4 (2013) 1432.
- [18] D.A. Wang, T. Hisatomi, T. Takata, C.S. Pan, M. Katayama, J. Kubota, K. Domen, Core/Shell photocatalyst with spatially separated co-catalysts for efficient reduction and oxidation of water, *Angew. Chem. Int. Ed.* 52 (2013) 11252–11256.
- [19] A.Y. Meng, L.Y. Zhang, B. Cheng, J.G. Yu, $\text{TiO}_2\text{-MnO}_x\text{-Pt}$ hybrid multiheterojunction film photocatalyst with enhanced photocatalytic CO_2 -reduction activity, *ACS Appl. Mater. Interfaces* 11 (2018) 5581–5589.
- [20] L.C. Mu, Y. Zhao, A.L. Li, S.Y. Wang, Z.L. Wang, J.X. Yang, Y. Wang, T.F. Liu, R. Chen, J. Zhu, F.T. Fan, R.G. Li, C. Li, Enhancing charge separation on high symmetry SrTiO_3 exposed with anisotropic facets for photocatalytic water splitting, *Energy Environ. Sci.* 9 (2016) 2463–2469.
- [21] Y.B. Yan, J.W. Miao, Z.H. Yang, F.X. Xiao, H.B. Yang, B. Liu, Y.H. Yang, Carbon nanotube catalysts: recent advances in synthesis, characterization and applications, *Chem. Soc. Rev.* 44 (2015) 3295–3346.
- [22] Y. Lin, S.H. Wu, X. Li, X. Wu, C.P. Yang, G.M. Zeng, Y.R. Peng, Q. Zhou, L. Lu, Microstructure and performance of Z-scheme photocatalyst of silver phosphate modified by MWCNTs and Cr-doped SrTiO_3 for malachite green degradation, *Appl. Catal. B: Environ.* 227 (2018) 557–570.
- [23] X. Yuan, D. Floresyona, P.-H. Aubert, T.-T. Bui, S. Remita, S. Ghosh, F. Brisset, F. Goubard, H. Remita, Photocatalytic degradation of organic pollutant with polypyrrole nanostructures under UV and visible light, *Appl. Catal. B: Environ.* 242 (2019) 284–292.
- [24] J. Yang, X. Wang, B. Li, L. Ma, L. Shi, Y.J. Xiong, H.G. Xu, Novel iron/cobalt-containing polypyrrole hydrogel-derived trifunctional electrocatalyst for self-powered overall water splitting, *Adv. Funct. Mater.* 27 (2017) 1606497.
- [25] T.J. Yao, L. Shi, H. Wang, F.X. Wang, J. Wu, X. Zhang, J.M. Sun, T.Y. Cui, A simple method for the preparation of $\text{TiO}_2/\text{Ag}\text{-AgCl@Polypyrrole}$ composite and its enhanced visible-light photocatalytic activity, *Chem. Asian J.* 11 (2016) 141–147.
- [26] N.M. Dimitrijevic, S. Tepavcevic, Y. Liu, T. Rajh, S.C. Silver, D.M. Tiede, Nanostructured TiO_2 /polypyrrole for visible light photocatalysis, *J. Phys. Chem. C* 117 (2013) 15540–15544.
- [27] Y.H. Liang, X. Wang, W.J. An, Y. Li, J.S. Hu, W.Q. Cui, A g-C₃N₄@ppy-rGO 3D structure hydrogel for efficient photocatalysis, *Appl. Surf. Sci.* 466 (2019) 666–672.
- [28] V.-D. Dao, N.T.P. Le Chi, D. Van Thuan, T.-D. Pham, D.-T. Tran, M.P. Nguyen, P. Thao, M.V. Nguyen, N.T. Dieu Cam, N.M. Tuong, N.M. Dang, H.-S. Choi, Superior stability and photocatalytic activity of TaN₅ sensitized/protected by conducting polymers for water splitting, *J. Alloys Compd.* 775 (2019) 942–949.
- [29] Y. Lin, S.H. Wu, C.P. Yang, M. Chen, X. Li, Preparation of size-controlled silver phosphate catalysts and their enhanced photocatalysis performance via synergistic effect with MWCNTs and PANI, *Appl. Catal. B: Environ.* 245 (2019) 71–86.
- [30] Z. Bai, Q. Yang, J.L. Wang, Catalytic ozonation of dimethyl phthalate using Fe₃O₄/multi-wall carbon nanotubes, *Environ. Technol.* 38 (2016) 1–10.
- [31] D.P. Bhattarai, A.P. Tiwari, B. Maharjan, B. Tumurbaatar, C.H. Park, C.S. Kim, Sacrificial template-based synthetic approach of polypyrrole hollow fibers for photothermal therapy, *J. Colloid Interface Sci.* 534 (2019) 447–458.
- [32] D.J. Martin, N. Umezawa, X.W. Chen, J.H. Ye, J. Tang, Facet engineered Ag_3PO_4 for efficient water photooxidation, *Energ. Environ. Sci.* 6 (2013) 3380.
- [33] J. Zwara, E. Grabowska, T. Klimczuk, W. Lisowski, A. Zaleska-Medynska, Shape-dependent enhanced photocatalytic effect under visible light of Ag₃PO₄ particles, *J. Photochem. Photobiol. A* 367 (2018) 240–252.
- [34] Z.C. Zhuang, Y. Li, Z.L. Li, F. Lv, Z.Q. Lang, K.N. Zhao, L. Zhou, L. Moskaleva, S.J. Guo, L.Q. Mai, MoB/g-C₃N₄ interface materials as a schottky catalyst to boost hydrogen evolution, *Angew. Chem. Int. Ed.* 57 (2018) 496–500.
- [35] H. Wang, X.Z. Yuan, Y. Wu, X.H. Chen, L.J. Leng, H. Wang, H. Li, G.M. Zeng, Facile synthesis of polypyrrole decorated reduced graphene oxide-Fe₃O₄ magnetic composites and its application for the Cr(VI) removal, *Chem. Eng. J.* 262 (2015) 597–606.
- [36] J.A. Huítrón-Gamboa, J.C. Encinas, M.M. Castillo-Ortega, T.D. Castillo-Castro, H. Santacruz-Ortega, D.E. Rodríguez-Félix, O. Manero, Supercapacitor based on in situ chemical synthesis of polypyrrole on rubber substrate: preparation and characterization, *Polym. Bull.* 76 (2018) 1–17.
- [37] Y. Matsumoto, Energy positions of oxide semiconductors and photocatalysis with Iron complex oxides, *J. Solid State Chem.* 126 (1996) 227–234.
- [38] M. Trchova, J. Stejskal, Resonance Raman spectroscopy of conducting polypyrrole nanotubes: disordered surface versus ordered body, *J. Phys. Chem. A* 122 (2018) 9298–9306.
- [39] B.M. Hryniwicz, R.V. Lima, F. Wolfart, M. Vidotti, Influence of the pH on the electrochemical synthesis of polypyrrole nanotubes and the supercapacitive performance evaluation, *Electrochim. Acta* 293 (2019) 447–457.
- [40] H. Zhang, R.L. Zong, J.C. Zhao, Y.F. Zhu, Dramatic visible photocatalytic degradation performances due to synergistic effect of TiO_2 with PANI, *Environ. Sci. Technol.* 42 (2008) 3803–3807.
- [41] P.Y. Dong, Y.H. Wang, B.C. Cao, S.Y. Xin, L.N. Guo, J. Zhang, F.H. Li, Ag₃PO₄/reduced graphite oxide sheets nanocomposites with highly enhanced visible light photocatalytic activity and stability, *Appl. Catal. B: Environ.* 132–133 (2013) 45–53.
- [42] F. Chen, Q. Yang, J. Sun, F. Yao, S.N. Wang, Y.L. Wang, X.L. Wang, X.M. Li, C.G. Niu, D.B. Wang, G.M. Zeng, Enhanced photocatalytic degradation of tetracycline by AgI/BiVO₄ heterojunction under visible-light irradiation: mineralization efficiency and mechanism, *ACS Appl. Mater. Interfaces* 8 (2016) 32887–32900.
- [43] S.H. Wu, H.J. He, L. Xiang, C.P. Yang, G.M. Zeng, B. Wu, S.Y. He, L. Li, Insights into atrazine degradation by persulfate activation using composite of nanoscale zero-valent iron and graphene: performances and mechanisms, *Chem. Eng. J.* 341 (2018) 126–136.
- [44] H.J. He, Z.H. Xiang, X.J. Chen, H. Chen, H. Huang, M. Wen, C.P. Yang, Biosorption of Cd(II) from synthetic wastewater using dry biofilms from biotrickling filters, *Int. J. Environ. Sci. Technol.* 15 (2017) 1–10.
- [45] S. Valencia, J.M. Marin, G. Restrepo, F.H. Frimmel, Evaluation of natural organic matter changes from Lake Hohloh by three-dimensional excitation-emission matrix fluorescence spectroscopy during TiO_2/UV process, *Water Res.* 51 (2014) 124–133.
- [46] Y. Cheng, H.J. He, C.P. Yang, G.M. Zeng, X. Li, H. Chen, G. Yu, Challenges and solutions for biofiltration of hydrophobic volatile organic compounds, *Biotechnol. Adv.* 34 (2016) 1091–1102.
- [47] G.P. Sheng, H.Q. Yu, Characterization of extracellular polymeric substances of aerobic and anaerobic sludge using three-dimensional excitation and emission matrix fluorescence spectroscopy, *Water Res.* 40 (2006) 1233–1239.
- [48] S.H. Wu, H.R. Li, X. Li, H.J. He, C.P. Yang, Performances and mechanisms of efficient degradation of atrazine using peroxymonosulfate and ferrate as oxidants, *Chem. Eng. J.* 353 (2018) 533–541.
- [49] W.J. Wang, P. Xu, M. Chen, G.M. Zeng, C. Zhang, C.Y. Zhou, Y. Yang, D. Huang, C. Lai, M. Cheng, L. Hu, W.P. Xiong, H. Guo, M. Zhou, Alkali metal-assisted synthesis of graphite carbon nitride with tunable band-gap for enhanced visible-light photocatalysis, *Appl. Catal. B: Environ.* 242 (2019) 284–292.

- light-driven photocatalytic performance, *ACS Sustain. Chem. Eng.* 6 (2018) 15503–15516.
- [50] H. Guo, C.G. Niu, L. Zhang, X.J. Wen, C. Liang, X.G. Zhang, D.L. Guan, N. Tang, G.M. Zeng, Construction of direct Z-scheme $\text{AgI}/\text{Bi}_2\text{Sn}_2\text{O}_7$ nanojunction system with enhanced photocatalytic activity: accelerated interfacial charge transfer induced efficient Cr(VI) reduction, tetracycline degradation and *Escherichia coli* inactivation, *ACS Sustain. Chem. Eng.* 6 (6) (2018) 8003–8018.
- [51] J.B. Wang, D. Zhi, H. Zhou, X.W. He, D.Y. Zhang, Evaluating tetracycline degradation pathway and intermediate toxicity during the electrochemical oxidation over a $\text{Ti}/\text{Ti}_4\text{O}_7$ anode, *Water Res.* 137 (2018) 324–334.
- [52] S.N. Wei, H.J. He, Y. Cheng, C.P. Yang, G.M. Zeng, L. Kang, H. Qian, C.Y. Zhu, Preparation, characterization, and catalytic performances of cobalt catalysts supported on KIT-6 silicas in oxidative desulfurization of dibenzothiophene, *Fuel* 200 (2017) 11–21.
- [53] M.H. Khan, H. Bae, J.Y. Jung, Tetracycline degradation by ozonation in the aqueous phase: proposed degradation intermediates and pathway, *J. Hazard. Mater.* 181 (2010) 659–665.
- [54] C.P. Yang, H. Qian, X. Li, Y. Cheng, H.J. He, G.M. Zeng, J. Xi, Simultaneous removal of multicomponent VOCs in biofilters, *Trends Biotechnol.* 36 (2018) 673–685.
- [55] I. Dalmazio, M.O. Almeida, R. Augusti, T.M. Alves, Monitoring the degradation of tetracycline by ozone in aqueous medium via atmospheric pressure ionization mass spectrometry, *J. Am. Soc. Mass Spectrom.* 18 (2007) 679–687.
- [56] Y.Y. Bu, Z.Y. Chen, C. Sun, Highly efficient Z-Scheme $\text{Ag}_3\text{PO}_4/\text{Ag}/\text{WO}_{3-x}$ photocatalyst for its enhanced photocatalytic performance, *Appl. Catal. B: Environ.* 179 (2015) 363–371.
- [57] F. Chen, Q. Yang, X.M. Li, G.M. Zeng, D.B. Wang, C.G. Niu, J.W. Zhao, H.X. An, T. Xie, Y.C. Deng, Hierarchical assembly of graphene-bridged $\text{Ag}_3\text{PO}_4/\text{Ag}/\text{BiVO}_4(040)$ Z-scheme photocatalyst: an efficient, sustainable and heterogeneous catalyst with enhanced visible-light photoactivity towards tetracycline degradation under visible light irradiation, *Appl. Catal. B: Environ.* 200 (2017) 330–342.
- [58] L. Tang, C.Y. Feng, Y.C. Deng, G.M. Zeng, J.J. Wang, Y.N. Liu, H.P. Feng, J.J. Wang, Enhanced photocatalytic activity of ternary $\text{Ag}/\text{g-C}_3\text{N}_4/\text{NaTaO}_3$ photocatalysts under wide spectrum light radiation: the high potential band protection mechanism, *Appl. Catal. B: Environ.* 230 (2018) 102–114.
- [59] C.Y. Feng, Y.C. Deng, L. Tang, G.M. Zeng, J.J. Wang, J.F. Yu, Y.N. Liu, B. Peng, H.P. Feng, J.J. Wang, Core-shell $\text{Ag}_2\text{CrO}_4/\text{N-GQDs@g-C}_3\text{N}_4$ composites with anti-photocorrosion performance for enhanced full-spectrum-light photocatalytic activities, *Appl. Catal. B: Environ.* 239 (2018) 525–536.
- [60] Y. Yang, C. Zhang, D.L. Huang, G.M. Zeng, J.H. Huang, C. Lai, C.Y. Zhou, W.J. Wang, H. Guo, W.J. Xue, R. Deng, M. Cheng, W.P. Xiong, Boron nitride quantum dots decorated ultrathin porous $\text{g-C}_3\text{N}_4$: intensified exciton dissociation and charge transfer for promoting visible-light-driven molecular oxygen activation, *Appl. Catal. B: Environ.* 245 (2019) 87–99.
- [61] C.N. He, W.Q. Huang, L. Xu, Y.C. Yang, B.X. Zhou, G.F. Huang, P. Peng, W.M. Liu, Tuning near-gap electronic structure, interface charge transfer and visible light response of hybrid doped graphene and Ag_3PO_4 composite: dopant effects, *Sci. Rep.* 6 (2016) 22267.
- [62] W.Y. Zhai, G.P. Li, P. Yu, L.F. Yang, L.Q. Mao, Silver phosphate/carbon nanotube-stabilized pickering emulsion for highly efficient photocatalysis, *J. Phys. Chem. C* 117 (2013) 15183–15191.
- [63] H.J. Tang, C.M. Hessel, J.Y. Wang, N.L. Yang, R.B. Yu, H.J. Zhao, D. Wang, Two-dimensional carbon leading to new photoconversion processes, *Chem. Soc. Rev.* 43 (2014) 4281–4299.
- [64] C.P. Yang, H. Chen, G.M. Zeng, G.L. Yu, S.L. Luo, Biomass accumulation and control strategies in gas biofiltration, *Biotechnol. Adv.* 28 (2010) 531–540.